Volume 49
DOE/DP40200-188

LLE Review

Quarterly Report

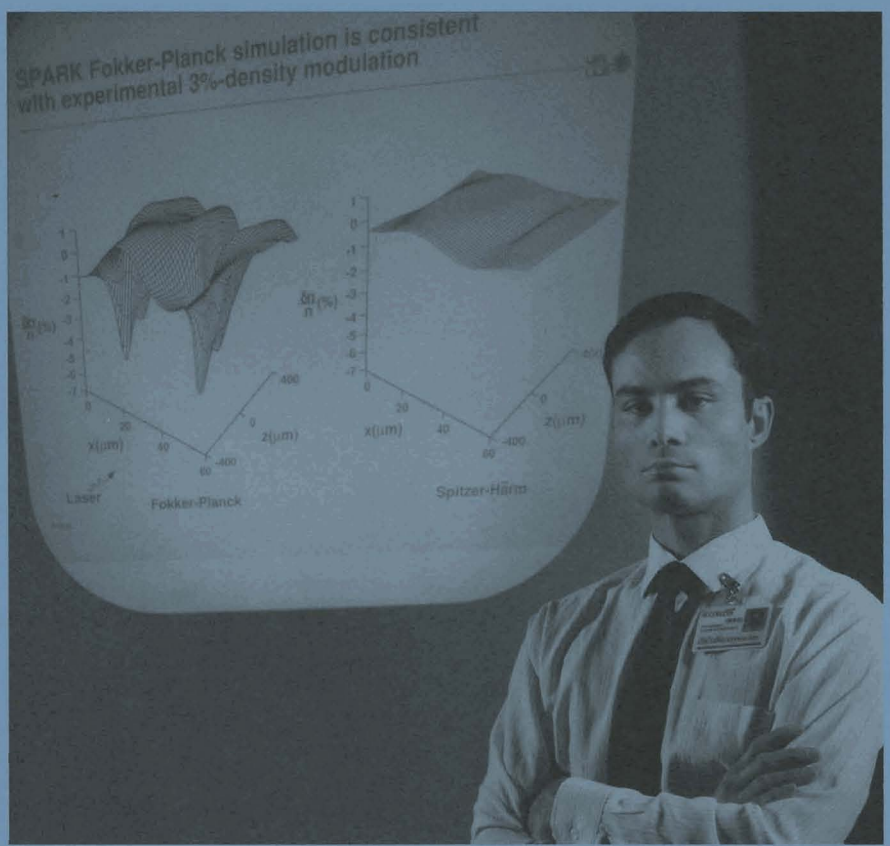

October–December 1991

Laboratory for Laser Energetics
College of Engineering and Applied Science
University of Rochester
250 East River Road
Rochester, New York 14623-1299

Volume 49
DOE/DP40200-188

LLE Review

Quarterly Report

Editor: R. L. Keck
(716) 275-0259

October–December 1991

Laboratory for Laser Energetics
College of Engineering and Applied Science
University of Rochester
250 East River Road
Rochester, New York 14623-1299

This report was prepared as an account of work conducted by the Laboratory for Laser Energetics and sponsored by New York State Energy Research and Development Authority, the University of Rochester, the U.S. Department of Energy, and other agencies.

Neither the above-named sponsors, nor any of their employees, makes any warranty, expressed or implied, or assumes any legal liability or responsibility for the accuracy, completeness, or usefulness of any information, apparatus, product, or process disclosed, or represents that its use would not infringe privately owned rights.

Reference herein to any specific commercial product, process, or service by trade name, mark, manufacturer, or otherwise, does not necessarily constitute or imply its endorsement, recommendation, or favoring by the United States Government or any agency thereof or any other sponsor.

Results reported in the LLE Review should not be taken as necessarily final results as they represent active research. The views and opinions of authors expressed herein do not necessarily state or reflect those of any of the above sponsoring entities.

IN BRIEF

This volume of the LLE Review, covering the period October–December 1991, contains articles on the analysis of argon-filled target experiments, and a theoretical analysis of the impact of nonlocal heat transport in laser filamentation in plasmas. In the Advanced Technology section there is an article on mechanisms that affect thin-film conductivity, and a report on the gain characteristics of the 20-cm SSA prototype amplifier to be used in the OMEGA Upgrade. Finally, the activities of the National Laser Users Facility and the GDL and OMEGA laser facilities are summarized.

Highlights of the research reported in this issue are

- Argon radiation from argon-filled, polymer-shell targets is used as a core-temperature diagnostic and density diagnostic of the surrounding region in a regime where the argon line radiation is strongly absorbed.
- A theoretical analysis of the impact of nonlocal heat transport on laser filamentation in plasmas is developed. The resulting model is compared with experimental observations and the implications for ICF are discussed.
- A study of thermal conductivity in thin films seeks to identify mechanisms that result in degradation of thin-film conductivity. Identifying these mechanisms can lead to changes in thin-film manufacture that will improve their resistance to laser damage.

- The gain characteristics of the 20-cm SSA prototype amplifier have been measured. The amplifier has been found to meet or exceed its design goals.

CONTENTS

		Page
IN BRIEF		iii
CONTENTS		v
Section 1	PROGRESS IN LASER FUSION	1
1.A	Interpretation of Recent Argon Experiments on OMEGA	1
1.B	Nonlocal Heat-Transport Effects on the Filamentation of Light in Plasmas	11
Section 2	ADVANCED TECHNOLOGY DEVELOPMENTS	24
2.A	Microstructural Control of Thin-Film Thermal Conductivity	24
2.B	Energy Transport in a Modern Disk Amplifier	40
Section 3	NATIONAL LASER USERS FACILITY NEWS	56
Section 4	LASER SYSTEM REPORT	58
4.A	GDL Facility Report	58
4.B	OMEGA Facility Report	59
PUBLICATIONS AND CONFERENCE PRESENTATIONS		

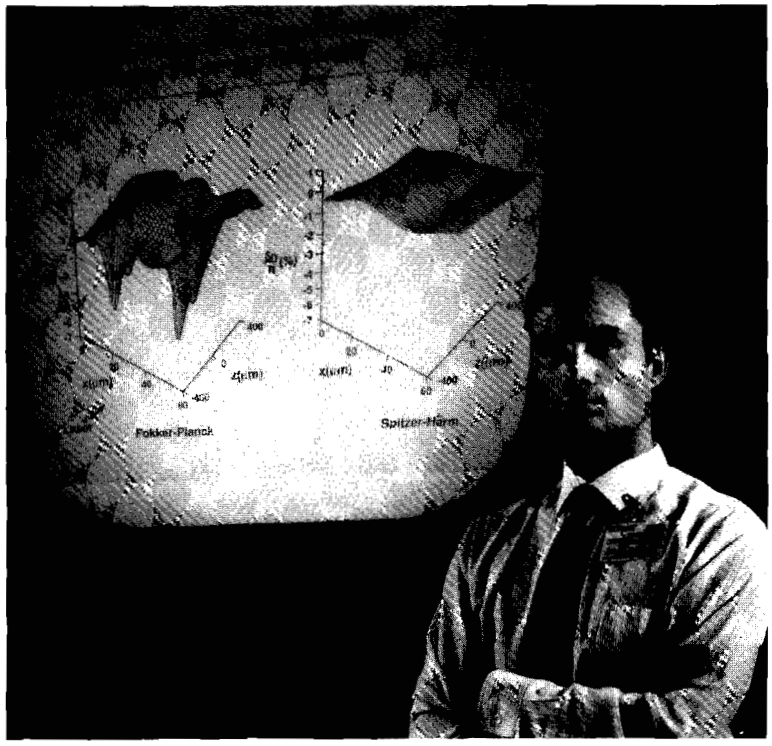

Eduardo Epperlein, Research Scientist, presents simulation results of laser filamentation based on the two-dimensional electron Fokker-Planck code SPARK. The code predictions have been successfully compared with filamentation experiments in underdense plasmas.

Section 1
PROGRESS IN LASER FUSION

1.A Interpretation of Recent Argon Experiments on OMEGA

Argon-filled polymer shell implosions are of interest because, unlike fuel-filled shells, they can be diagnosed using line-spectroscopy methods. In addition, the deceleration instability may be mitigated in these targets because of the high target-core density. Polymer shells have the important advantage over glass targets in that they attenuate argon lines to a much lesser extent. However, recent experiments have shown that the argon lines are very strongly absorbed by a cooler argon plasma surrounding the core. Therefore, the density diagnostics of the core are lost. However, we show here that the absorption can in turn be used to diagnose that cooler argon region. We also show that radiation at wavelengths away from absorption lines is little attenuated by the cooler argon, and it can yield information about the hot core, primarily its temperature.

Four regions in an imploded argon-filled CH shell are shown schematically in Fig. 49.1. The regions are (a) the hot central core, emitting a strong continuum, (b) a cooler argon region surrounding the core, where the absorption lines in partially ionized argon are formed; the helium-like and hydrogen-like argon lines emitted in region (a) are also strongly absorbed here, (c) the compressed, low-temperature part of the polymer shell, and (d) the ablated, laser-heated part of the polymer shell.

Hydrodynamic mixing between adjacent target regions may adversely affect target performance, and some evidence to that effect, in the existing data, will be described.

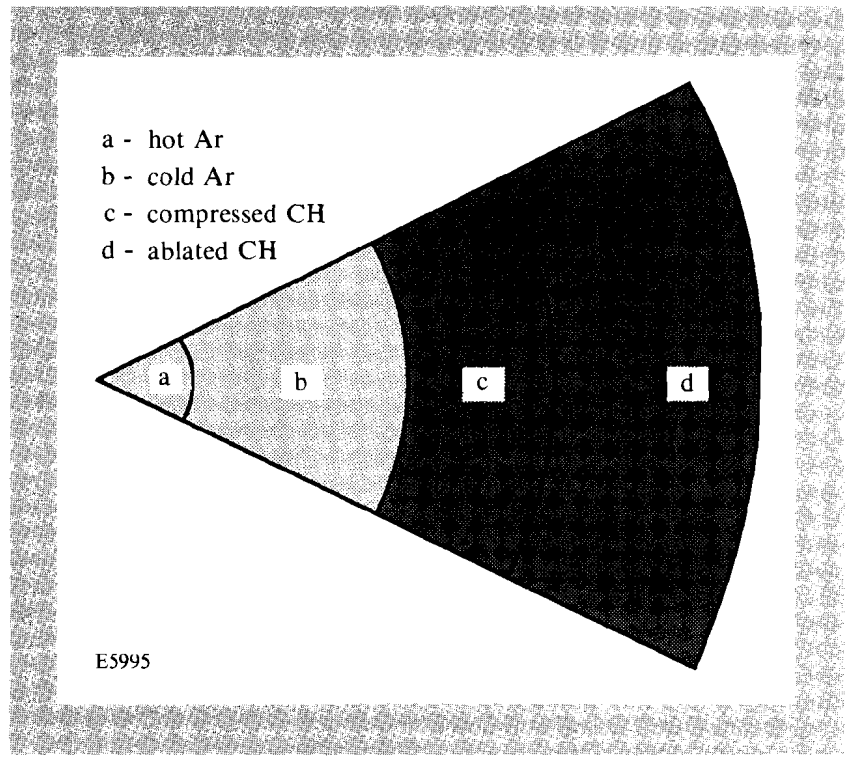

Fig. 49.1
Schematic representation of relevant regions in the argon-filled CH shell target. Argon lines emitted in region (a) are absorbed within region (b).

The data is from a series of shots taken as a part of NLUF experiments conducted by C. F. Hooper of the University of Florida (jointly with an LLE group) and reported in Ref. 1. In these experiments, argon-filled plastic shells of diameter 250 μm and thicknesses of 6, 8, 10, and 12 μm were imploded with 600-ps FWHM, 1200-J laser pulses. The targets were filled with 20 atm of argon and were coated with 0.05 μm of aluminum. The 24 OMEGA beams were smoothed by spectral dispersion[2] (SSD) at a frequency of 8.45 MHz with a bandwidth $\Delta\lambda/\lambda = 2.7 \times 10^{-4}$. The results are shown in Figs. 49.2 and 49.3. Figure 49.2 shows the time-integrated spectra for shots 20876, 20878, 20882, and 20886. The experimental parameters for these shots were similar, except for the shell thicknesses of 6, 8, 10, and 12 μm, respectively. Figure 49.3 shows the streaked spectrum for shot 20878 (8-μm thickness).

Absorption Lines in Argon Ions

The most striking feature in these figures is the absorption lines in the range 2.9–3.1 keV, formed within the continuum emitted by the hot target core. These lines are due to 1s–2p transitions in argon ions having n electrons ($n = 0$–7) in the L shell. They have been used in the past[3,4] to determine the $\rho\Delta r$ of the absorption region within the shell. Here, the absorption region is within the fill gas rather than the shell (the CH shell has no absorption lines because it is mostly stripped of electrons; even if it were not stripped, the strong photoionization absorption at the low-energy position of the carbon lines would wipe out any line-absorption features). The absorption in argon is strong enough to cause extinction, i.e., in the region of flat spectrum (around 3.05 keV) essentially all the core-emitted photons are absorbed on the way out. In that case, only a lower bound on the $\rho\Delta r$ of the absorption region can be obtained.

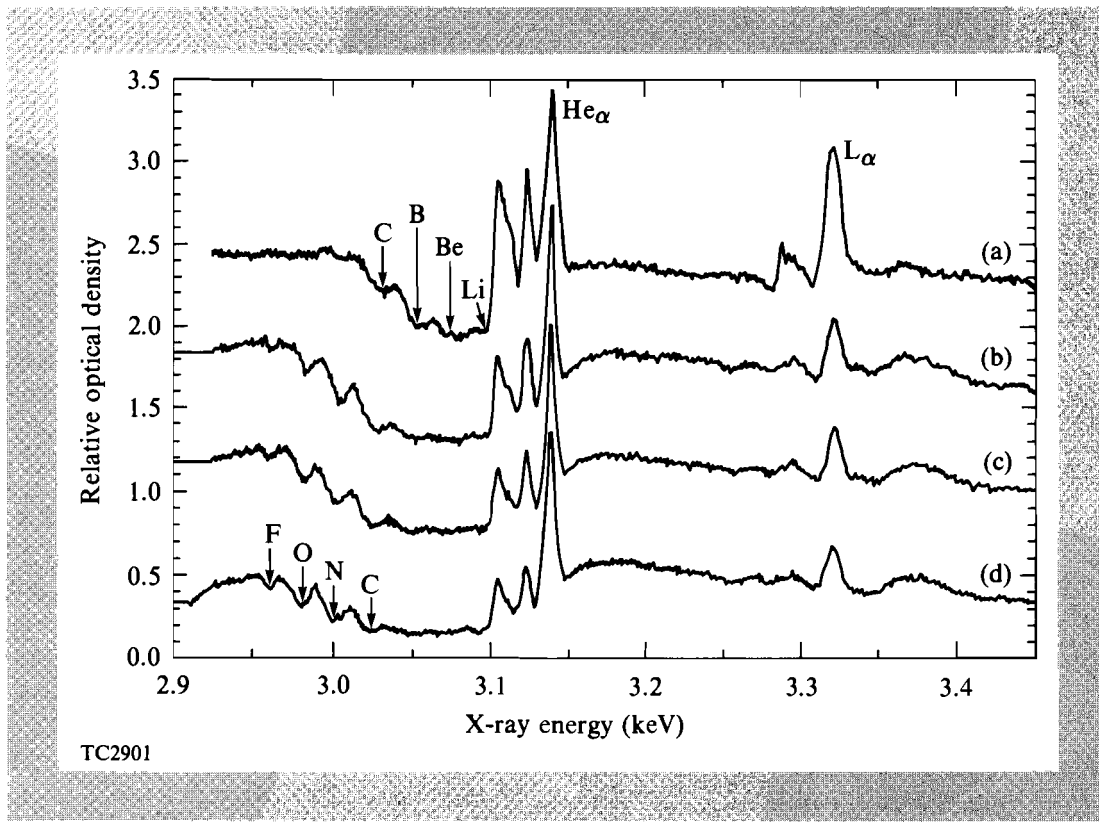

Fig. 49.2
Time-integrated spectra for shots 20876, 20878, 20882, and 20886. The experimental parameters for these shots were similar, except for shell thicknesses of 6, 8, 10, and 12 μm, respectively. The four spectra are shifted vertically for clarity. The zero (i.e., film background) level for these spectra is essentially that of the lowest density around 3.08 keV.

The temperature in the absorption region can only be estimated because of the extinction caused by strong line absorption. When the $\rho\Delta r$ of the absorbing layer is sufficiently small, the intensity contour of the group of absorbing lines is obtained, which yields the distribution of charge states, hence the temperature. In fact, a similar absorption manifold within a thin layer in the shell[4] had no extinction and enabled us to estimate the temperature in the cold part of the shell. A more precise determination of the temperature of the absorption layer in the present case may become possible with a lower argon fill pressure, which will reduce the absorption in these lines.

The progression to thicker shells in Fig. 49.2 [curves (a)–(d)] indicates an increasing $\rho\Delta r$ of the absorbing region [(b) in Fig. 49.1]. This is evidenced by the observation that at any wavelength, the emitted intensity goes down with increasing shell thickness, until extinction is reached. However, code simulations for these experiments have shown[1] that the total argon $\rho\Delta r$ should decrease with increasing shell thickness. This point should be further studied; it could be that because the temperature falls with increasing shell thickness, the total argon $\rho\Delta r$ decreases even as the $\rho\Delta r$ of the cold layer increases.

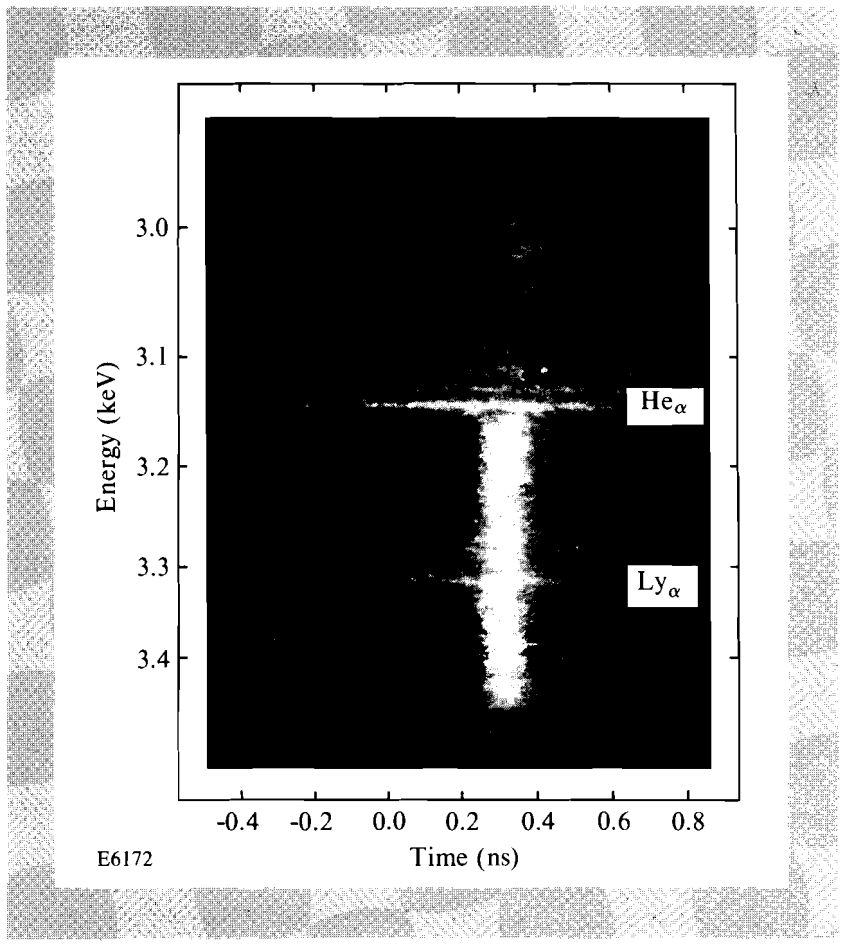

Fig. 49.3
Streaked spectrum for shot 20878 (CH shell of 8-μm thickness). The time scale zero is arbitrary. The narrow argon lines are emitted by the argon enclosed within the polymer shell. Around peak compression, a strong continuum is emitted at energies higher than about 3.15 keV; absorption by argon ions cuts its intensity at lower photon energies.

We next estimate a lower bound on the $\rho\Delta r$ of the argon absorption layer, using the equation[4]

$$\rho\Delta r = \frac{m c M_i}{f \pi e^2 \alpha} \int \ln \frac{I_o}{I_\nu} d\nu \, . \tag{1}$$

Here M_i is the ionic mass, α is the fraction of the ions in the ground state, I_o is the unabsorbed intensity level (read outside the spectral region of absorption lines at, say, 2.95 keV), and the integral is over the intensity I_ν of each absorption line. The absorption oscillator strength f has to be averaged over the lower-state levels as well as summed over the upper-level states (of which there can be a few tens,[4] within each absorption line in Fig. 49.2). Equation (1) gives the $\rho\Delta r$ of one ionic species, using a single absorption line in Fig. 49.2; the total $\rho\Delta r$ is obtained by summing the (deconvolved) contributions from all the observed absorption lines. For lines showing extinction (i.e., a flat intensity level) a lower bound on the corresponding $\rho\Delta r$ is obtained by assuming that they just broaden enough to merge with their neighboring lines. Using this procedure we estimate $\rho\Delta r \geq 3.2$ mg/cm^2. Two correction factors need to be applied, one is a finite-temperature correction[5] and the other a fluorescence correction.[6] Both corrections increase the estimated $\rho\Delta r$ and the corrected estimate becomes $\rho\Delta r \geq 5$ mg/cm^2.

To compare this estimate with the simulation results, we show in Fig. 49.4 the predicted temperature and density profiles for shot 20886 [spectrum (d) in Fig. 49.2]. The range of temperatures $T \leq 500$ eV is consistent with the ionization of argon ions up to the He-like charge state; thus, this is where the absorption lines of Fig. 49.2 would be formed. According to Fig. 49.4 the absorbing region extends from a radius of 15 μm outwards, and its $N_e\Delta r$ value is $\sim 1 \times 10^{21}$ cm^{-2}. For an average ionization of $Z = 14$ (B-like argon), this corresponds to $\rho\Delta r = 4.7$ mg/cm^2, in good agreement with the value estimated from the experiment. A detailed atomic-population calculation should improve the precision of the predicted $\rho\Delta r$.

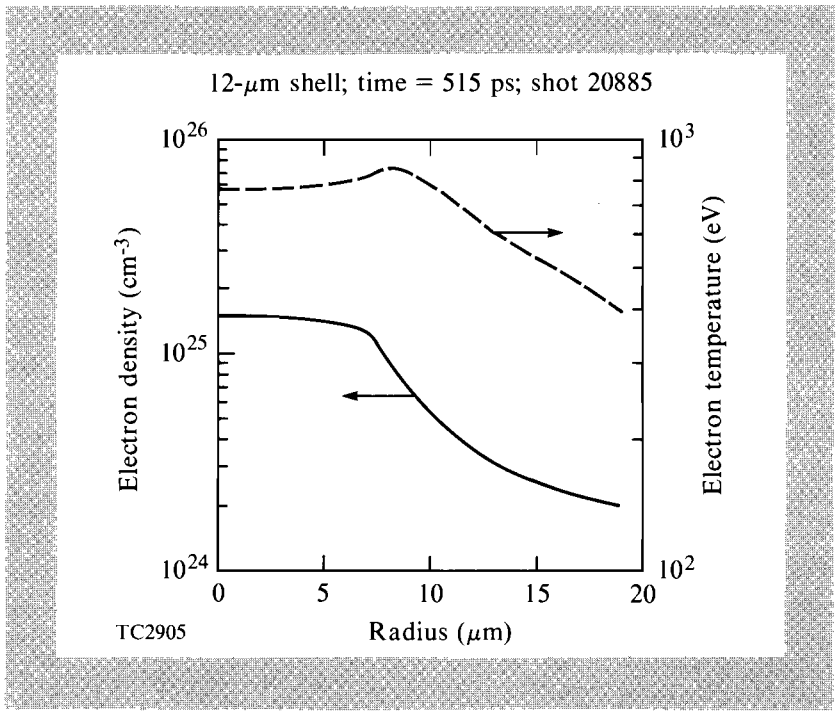

Fig. 49.4
The predicted temperature and density profiles for shot 20886 [spectrum (d) in Fig. 49.2]. The temperature gradient gives rise to the layer classification of Fig. 49.1.

An additional interesting feature related to the absorption lines is seen in the time-resolved data of Fig. 49.3. Around the time of peak compression there is a strong flare-up of continuum radiation at energies above the He_α line, caused by an increase in both the temperature and the density of the argon core. The absorption lines of Fig. 49.2 are seen in Fig. 49.3 for a brief period of time following peak compression (defined as the time of maximum continuum intensity). Obviously, when the continuum decays because of target expansion and cooling, the absorption lines should also disappear. However, Fig. 49.3 shows their appearance lags behind the onset of rise in the continuum intensity. When the continuum is already intense but the absorption lines have not yet appeared, the absorption is sufficiently high to cause extinction of all radiation, even at wavelengths between the absorption lines. As a comparison, Fig. 49.5 shows two predicted time-resolved spectra in the spectral range where the absorption lines appear. The figure shows that indeed the absorption lines should appear only after a complete extinction at the time of peak compression. The time difference between the two spectra in Fig. 49.5 is 38 ps; this is consistent with

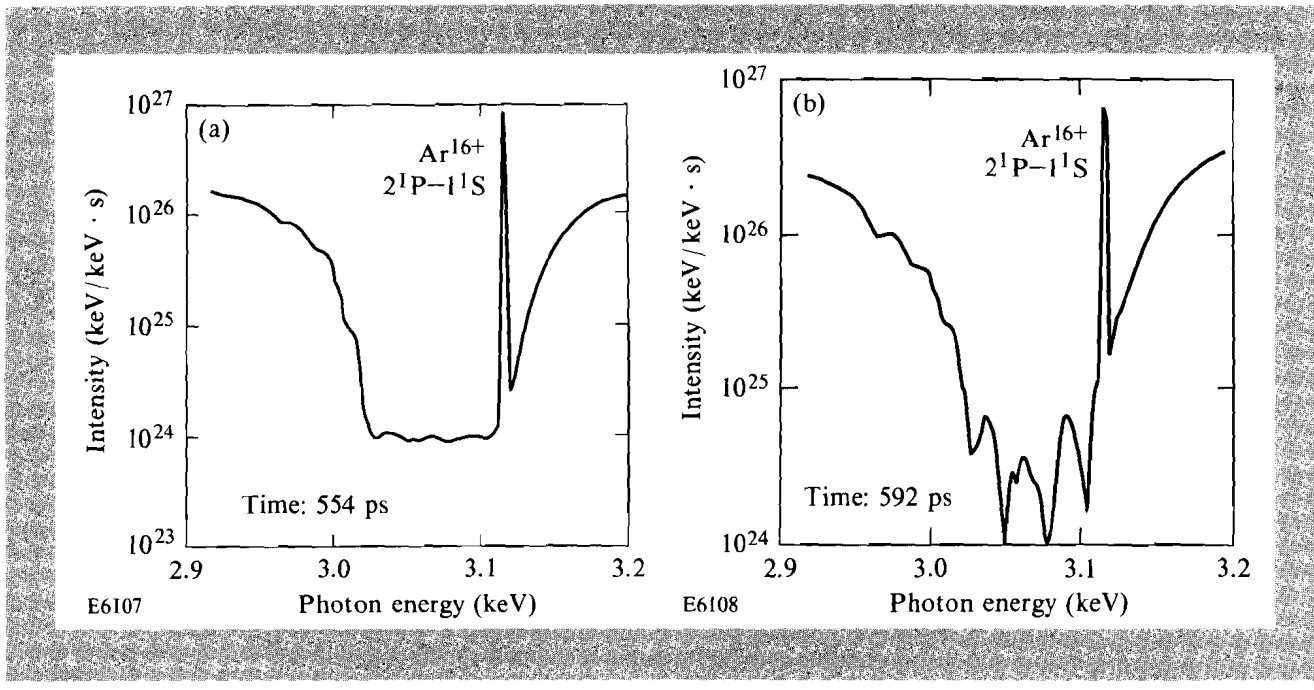

Fig. 49.5
The *LILAC*-predicted time-resolved spectra, in the spectral range where the absorption lines appear: (a) at the time 554 ps after the peak of the pulse, and (b) 38 ps later. Good agreement is seen with the experimental data of Fig. 49.3: complete absorption in the spectral range 3.0–3.1 keV, followed by the appearance of absorption lines.

Fig. 49.3, where the time of complete extinction precedes the time of absorption-line appearance by $\lesssim$ 80 ps. A close examination of the code results shows that this decrease in absorption is caused by the shock reflection at the target center. When the converging shock reaches the center [about the time of Fig. 49.5(a)], the hot central core becomes surrounded by a cooler, absorbing argon. However, at the time of Fig. 49.5(b), the reflected shock reaches the peripheral argon layer and heats it, thereby reducing its absorptivity.

Helium-like and Hydrogen-like Argon Lines

The lines of helium-like and hydrogen-like argon, unlike the lines studied in the preceding section, can appear in absorption as well as in emission. Thus, these lines represent a special case. They are emitted in plasma regions where the temperature is high enough for the excitation by electron collisions of 1s–2p transitions, which leads to 2p–1s spontaneous line emission. On the other hand, the ions with some electrons in the *L*-shell (Li-like and lower ionizations) exist in low-enough temperature regions, where electrons cannot excite 1s–2p transitions. However, the continuum radiation from the hot core can excite these transitions, thus forming the observed absorption lines. The resulting emission following such excitation (or fluorescence) merely causes a small reduction in the depth of the absorption features.[6]

The diagnosis based on helium-like and hydrogen-like argon lines is further complicated by the existence of argon in the CH shell. In fact, the strong and narrow emission argon lines in Figs. 49.2 and 49.3 are deemed to be emitted

mainly by the argon in the polymer shell, rather than by the argon fill gas. This conclusion follows from the observation in Fig. 49.3 that the intensity of these lines peaks earlier than peak compression, and that even for a modest compression they would have been much broader (see the following) if originating from the argon fill gas. If the argon emission lines in Figs. 49.2 and 49.3 are indeed emitted primarily in the shell, then subtracting them out leads to the conclusion that the argon lines emitted by the core are absorbed by the cooler argon layer [region (b) in Fig. 49.1], thus do not emanate from the target. This is indeed the predicted behavior, as seen in Fig. 49.6, showing the calculated spectrum around peak compression for the 12-μm-thick shell implosion. Argon fill gas was assumed to uniformly fill the shell, including the wall. The argon in the wall gives rise to emission lines, which appear very narrow because of the lower $\rho\Delta r$ in the shell. These narrow lines are superimposed on Stark-broadened argon lines that appear in absorption, because even the continuum at the wavelengths of the argon lines is absorbed by the cooler argon layer. The predicted (Fig. 49.6) and measured (Fig. 49.2) argon lines compare quite well, especially when we allow for the instrumental broadening of the argon lines from the shell, which was not included in the simulation of Fig. 49.6. In particular, curve (d) in Fig. 49.2 shows what appears to be the high-energy wing of an absorbed He_α line (around 3.15 keV). This is an indication of broad absorption profiles of argon resonance lines, which are masked by the emission of narrow lines from the argon in the shell; this is particularly the case for the He_α line.

A more conclusive measurement will be attempted with the He_β line at 3.68 keV, which was outside the range of the spectra in Figs. 49.2 and 49.3. As Fig. 49.6 shows, the Stark broadening of this line is much larger. Measuring this

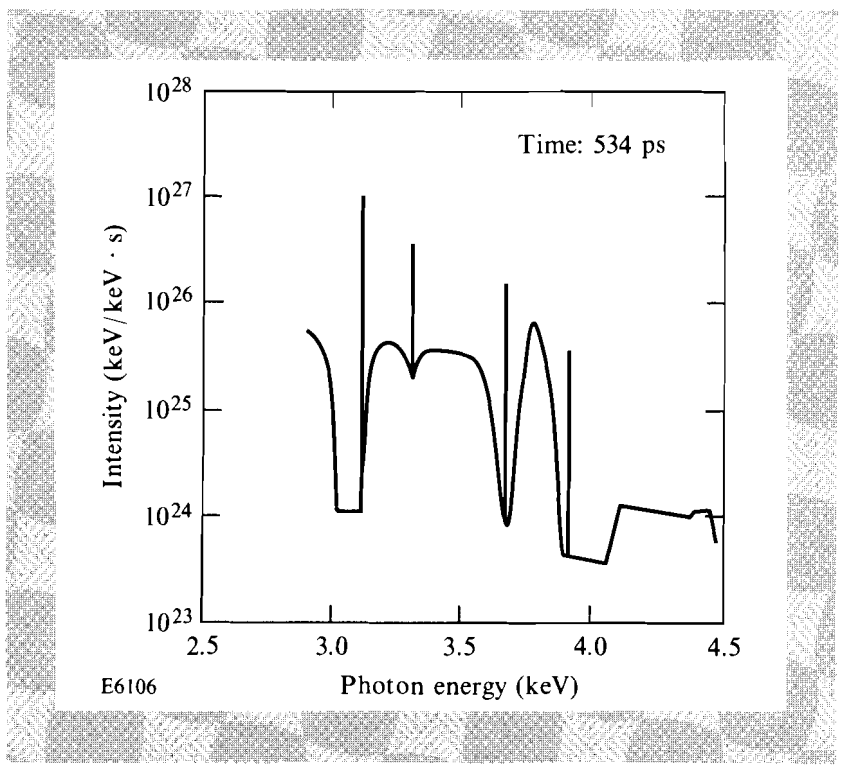

Fig. 49.6
The calculated spectrum around peak compression for the 12-μm-thick shell implosion. Argon fill gas was assumed to uniformly fill the shell, including the wall. The code correctly replicates the absorption in the spectral range 3.0–3.1 keV (see Fig. 49.2) as well as the narrow line emission caused by argon trapped within the polymer shell.

line profile could have demonstrated the existence of two distinct line-profile components: narrow emission line coming from the shell, and a broad profile formed in the cooler argon layer. The density in the absorption region can then be directly determined from the absorption Stark profile.

It is interesting to compare the results discussed here with an earlier experimental series where argon-filled polymer shells were also used.[7] In that series, bigger and thinner shells were imploded with a higher-energy laser, which was not smoothed by spectral dispersion (but DPP's were employed). Typically, shells of diameter 420 μm and thickness 6 μm were filled with 10-atm argon fill pressure and imploded with 1700-J laser pulses of 680-ps FWHM. An overcoat layer of 0.05-μm Al was also applied to the targets. There is a striking difference between the results in that series and those of Fig. 49.3. There (Fig. 2 of Ref. 7), strong and broad argon lines appear in emission, whereas such lines are missing completely in Fig. 49.3. In the code-calculated spectrum for the conditions of Ref. 7, the He_α line is predicted to be totally absorbed (except for a narrow-line emission from the shell). This striking disagreement with the code may be because of mixing of target layers (a) and (b) (Fig. 49.1) in that earlier series of experiments. To observe absorption lines, the hot core should be totally surrounded by the cooler layer, and mixing of the two layers enables the inner radiation to escape with little absorption. On the other hand, both the He_α and the Ly_α core-emitted lines in Figs. 49.2 and 49.3 agree with the predictions of Fig. 49.6, after subtracting out the narrow lines caused by the argon in the shell: both appear in absorption.

Argon Core Continuum Emission and Absorption

In addition to the spectral-line diagnosis described previously, the continuum emission and absorption can also be a source of information. The continuum emitted by the hot argon core [region (a) in Fig. 49.1] can be absorbed on its way out, primarily in region (b). Absorption on 1s–2p transitions leading to the appearance of absorption lines in the spectrum was dealt with previously. Here we turn to continuum absorption, primarily caused by the photoelectric effect.

The total continuum absorption in cold argon in the range 2.8–3.5 keV is shown in Fig. 49.7. Below the *K*-edge at 3.2 keV the continuum absorption is insignificant in comparison with the line absorption in the same spectral region. However, there is no line absorption below the F-like absorption peak around 2.96 keV, because for Ne-like and lower ionizations, no 1s–2p transition into the full *L*-shell is possible. Because of the rise in continuum bound-free absorption towards lower photon energies (like ν^{-3}), at some point below 2.95 keV the absorption in the cool argon layer will be strong enough to cause the observed continuum (emitted by the hot argon core) to start declining. In Fig. 49.2 it appears as if that indeed is the case for the 12 μm shell. However, because of overlap of spectra caused by reflection from different crystal planes, no firm conclusion can be drawn. We can estimate the expected attenuation at 2.9 keV, within the cool argon layer, based on the $\rho\Delta r$ for that layer, as estimated previously. The opacity of cold argon at 2.9 keV is 190 cm^2/g. Since the *L*-shell of ions in the absorption layer is on the average half empty (the sequence of species corresponding to the absorption lines in Fig. 49.2 have

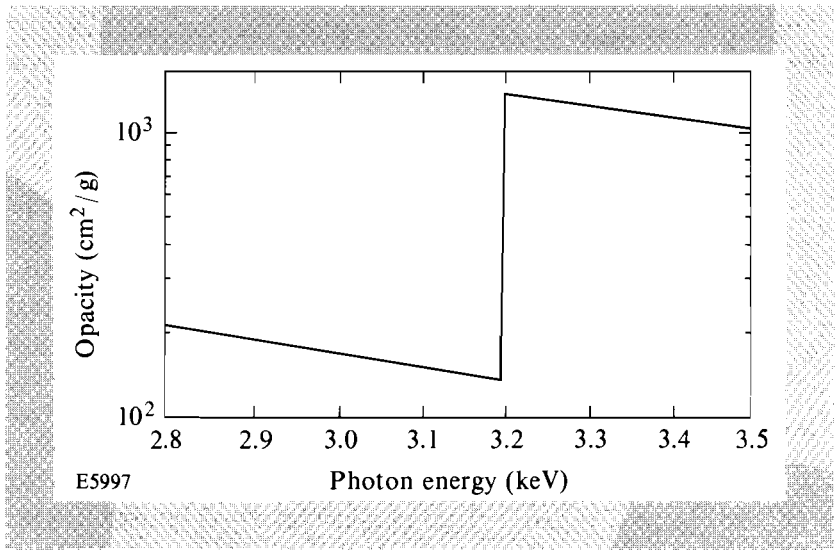

Fig. 49.7
The total continuum absorption in cold argon in the range 2.8–3.5 keV. The strong continuum observed above 3.2 keV (Fig. 49.3) is because of the ionization of the argon in region (b) of Fig. 49.1.

from 2 to 7 electrons in the *L*-shell). Thus, the opacity at 2.9 keV is ~95 cm^2/g, and the $\rho\Delta r$ of 5 mg/cm^2 gives an attenuation by a factor of $\exp(-0.47) = 0.6$.

Above the *K*-edge, the opacity of cold argon increases abruptly (Fig. 49.7) but the core-emitted continuum is nevertheless very intense (see Fig. 49.3). This indicates that very little of the argon in the cool layer is cool enough to be neutral. To further explain this, we start by determining the positions of the *K*-edges for argon ions. Since they are not tabulated in the literature, we rely on published[8] K_α line energies in ionized argon. As an example, the method of determining the *K*-edge energies is shown schematically in Fig. 49.8 for the Be-like argon ion. The energy difference between the states (A) and (B) is just the tabulated[8] K_α line energy for Li-like argon; the energy difference between states (B) and (C) is the tabulated[9] ionization energy of Be-like argon. Thus, by adding the two we obtain the energy difference between (A) and (C), i.e., the *K*-edge energy for Be-like

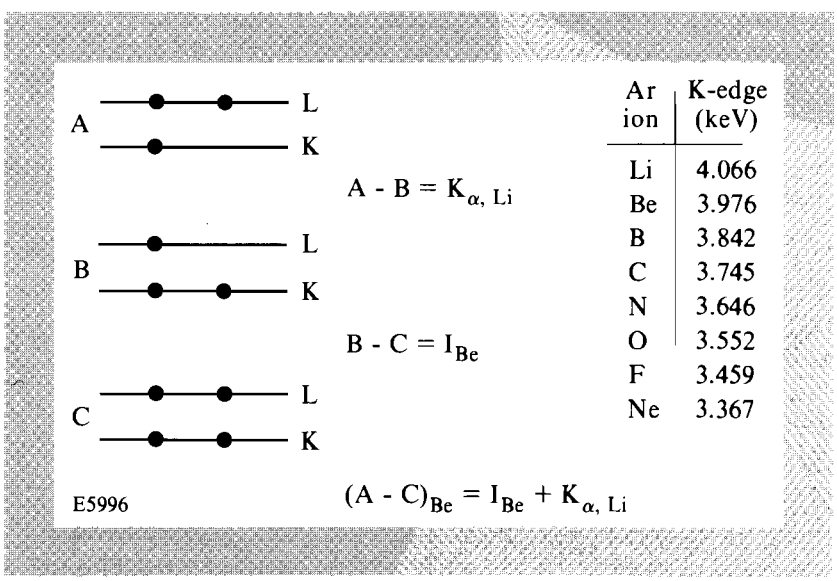

Ar ion	K-edge (keV)
Li	4.066
Be	3.976
B	3.842
C	3.745
N	3.646
O	3.552
F	3.459
Ne	3.367

Fig. 49.8
Schematic representation of the method of determining the *K*-edge energies of argon ions (here, the Be-like argon).

argon. The tabulated results in Fig. 49.8 show that for all the argon ions known to exist in the absorbing layer (i.e., F-like and higher ionizations), the corresponding K-edges fall outside the spectral range of Fig. 49.2. Thus, if no lower ionizations than F-like exist in the shell (which would be true if the shell temperature is at no place lower than ~50 eV), no K-shell photoionization absorption will occur in the spectral range of Fig. 49.2. Extending the measurement to higher photon energies than those of Fig. 49.2 may not reveal the absorption edges corresponding to these K-edges either. This is because the absorption is divided among the various argon-ionic species, each having an edge at a different spectral location. The opacity above the cold K-edge (Fig. 49.7) is ~10^3 cm^2/g, which for a $\rho\Delta r$ of 5 mg/cm^2 would yield an attenuation by a factor exp(−5); however, divided among, say, 10 species, the attenuation at any edge will only be about exp(−0.5). It should be noted that the increase in continuum intensity near 3.35 keV is instrumental and is caused by an increase in film sensitivity (the LIII edge of silver is at 3.35 keV).

Based on the previous conclusion that target region (b) (in Fig. 49.1) is quasi-transparent to the continuum for energies above ~3.15 keV, the temperature of the hot argon core can be determined through the slope of the observed continuum emission in that spectral region. Figure 49.2 indicates that the temperature falls for increasing shell thickness, as predicted; however, a more quantitative temperature determination should await the overcoming of the crystal reflection overlap problem. Coupled with this temperature determination, the relative intensity of the continuum can be used to estimate the change in the ρr of the hot argon core region, for increasing shell thickness.

In conclusion, the diagnosis (with argon spectroscopy) of compressed targets having core-temperature gradients requires special care. In the case of high fill pressure of argon (several atmospheres), the argon lines will appear in absorption and yield information on the conditions (primarily the density and the $\rho\Delta r$) of the peripheral argon layer. On the other hand, the continuum radiation can yield information on the conditions (primarily the temperature) of the central argon core. For an argon fuel mixture where the argon constitutes a sufficiently small fraction, the argon lines will appear in emission and provide diagnostics information on the conditions of the central core.

ACKNOWLEDGMENT

This work was supported by the U.S. Department of Energy Office of Inertial Confinement Fusion under agreement No. DE-FC03-85DP40200 and by the Laser Fusion Feasibility Project at the Laboratory for Laser Energetics, which is sponsored by the New York State Energy Research and Development Authority and the University of Rochester.

REFERENCES

1. J. Delettrez, R. Epstein, D. K. Bradley, P. A. Jaanimagi, R. C. Mancini, and C. F. Hooper, Jr., "Hydrodynamic Simulation of Non-LTE Atomic Physics of High-Density Implosions of Ar-filled Polymer Shell Targets," in the *Proceedings of the International Workshop on Radiative Properties of Hot Dense Matter*, Sarasota, FL, 22–26 October 1990.
2. S. Skupsky, R. W. Short, T. Kessler, R. S. Craxton, S. Letzring, and J. M. Soures, J. Appl. Phys. **66**, 3456 (1989).

3. B. Yaakobi, R. L. McCrory, S. Skupsky, J. A. Delettrez, P. Bourke, H. Deckman, C. F. Hooper, and J. M. Soures, Opt. Commun. **34**, 213 (1980).

4. LLE Review **22**, 51 (1985).

5. R. Epstein, Phys. Rev. A **43**, 961 (1991).

6. R. Epstein and B. Yaakobi, Phys. Rev. A **44**, 5111 (1991).

7. C. F. Hooper, Jr., D. P. Kilcrease, R. C. Mancini, L. A. Woltz, D. K. Bradley, P. A. Jaanimagi, and M. C. Richardson, Phys. Rev. Lett. **63**, 267 (1989).

8. L. L. House, Astrophys. J. Suppl. Ser. 155 **18**, 21 (1969).

9. T. A. Carlson *et al.*, Atomic Data **2**, 63 (1970).

1.B Nonlocal Heat-Transport Effects on the Filamentation of Light in Plasmas

Laser filamentation is potentially a serious problem for future inertial-confinement-fusion (ICF) schemes that produce long-scale-length plasmas.[1] The filamentation process occurs as a result of spatial variations in the incident laser irradiation on target that form self-focusing density channels along the direction of propagation. The instability is referred to as ponderomotive[2] or thermal,[3] depending on whether the density channels are created primarily by ponderomotive or thermal forces. Some undesirable consequences of filamentation are the triggering of parametric instabilities and the production of nonuniform ablation pressures in direct-drive ICF.

A recent kinetic analysis of filamentation has shown that the thermal mechanism dominates over the ponderomotive mechanism for most cases of interest to ICF.[4] This result comes from a reduction in the electron thermal conductivity for temperature variations over distances shorter than about 200 λ_e, where

$$\lambda_e = T^2 / \left[4\pi n e^4 (Z+1)^{1/2} \ln\Lambda \right]$$

is the delocalization length, or mean free path, of a thermal electron (T is the electron temperature, n is the electron number density, e is the magnitude of the electron charge, Z is the ionization number, and $\ln\Lambda$ is the Coulomb logarithm). A reduced thermal conductivity results in larger temperature modulations, driving larger density modulations and enhancing the instability. This analysis has since been confirmed by 2-D Fokker-Planck (FP) simulations, using the SPARK code,[5] which also reproduce well the filamentation experiments performed by Young *et al.* (1988).[6] Successful comparisons between SPARK simulations and experiments also provide indirect evidence of flux inhibition in a laser-fusion plasma corona.

The aim of this article is to (a) improve our understanding of nonlocal heat transport and check the accuracy of the reduced form of the FP equation used in our analysis, (b) review and improve the kinetic theory of laser filamentation, (c) provide a comparison between 2-D SPARK simulations and recent filamentation experiments by Young (1991),[7] and (d) discuss the implications of laser filamentation for the design of future ICF targets. The main conclusions are then presented.

Nonlocal Heat Transport

It is well known that for strong temperature gradients, such as are found in ICF plasmas, the electron heat flow can become inhibited when compared with the classical value[8] $\mathbf{q}_{SH} = -\kappa_{SH}\nabla T$ [where κ_{SH} is the classical Spitzer-Härm[9] (SH) heat conductivity]. One popular solution to this problem has been to limit the SH heat flow to some fraction f of the "free-streaming" heat flow $q_f = nm\upsilon_t^3$ (where m is the electron mass and $\upsilon_t = \sqrt{T/m}$), by setting $\mathbf{q} = \mathbf{q}_{SH} / \left(1 + |\mathbf{q}_{SH}|/fq_f\right)$.[10]

A more subtle, yet important, heat-flow reduction effect has been shown to arise even for arbitrarily small levels of heat flow $\left(\text{i.e., } |\mathbf{q}_{SH}| << fq_f\right)$,[11] provided the corresponding spatial temperature-modulation wavelength $\lambda_\perp$ is less than about $200\,\lambda_e$.[4,12] The appropriate reduction in the heat conductivity has been recently calculated for the case where a spatially modulated inverse-bremsstrahlung heating source is balanced by heat conduction in a homogeneous plasma with fixed ions.[4] More specifically, SPARK has been used to calculate the effective heat conductivity κ, defined by the the energy balance equation $k_\perp^2\,\kappa\delta T = \delta S$, where $k_\perp\left(= 2\pi/\lambda_\perp\right)$ is the modulation wave number, and δT and δS are the amplitudes of the temperature and heat source modulations, respectively. The result of the calculations are shown in Fig. 49.9, where we plot κ/κ_{SH} as a function of $k_\perp\lambda_e$. As expected, in the collisional limit $\left(k_\perp\lambda_e \to 0\right)$ $\kappa \to \kappa_{SH}$.

The strong reduction in conductivity when $k_\perp\lambda_e \gtrsim 0.03$ is because there are two main groups of electrons: a thermal group, which is representative of the plasma temperature, where most of the collisional heating (caused by inverse bremsstrahlung) is absorbed; and a suprathermal group, with velocities close to $3.7\,\upsilon_t$, which is responsible for carrying most of the heat flow.[8] In fluid theory, these two groups are assumed to be coupled by a single Maxwellian electron distribution in velocity. However, in practice, if the characteristic mean free path of the heat-carrying group is longer than the relevant spatial scale length ($\lambda_\perp$ in our case), these electrons will become decoupled from their thermal counterpart and establish a uniform distribution in configuration space. The reduction in the spatial gradient of the electrons at $3.7\,\upsilon_t$ will then lead to a reduction in the effective heat conductivity. Since the mean free path of an electron is proportional to υ^4 it is not surprising that this nonlocal transport effect becomes important for $\lambda_\perp \lesssim 200\,\lambda_e$ (instead of $\lambda_\perp \lesssim \lambda_e$, where λ_e is defined for a thermal electron).

In order to obtain more insight into the heat-flow process, let us first consider the Legendre expansion of the electron distribution function in one dimension

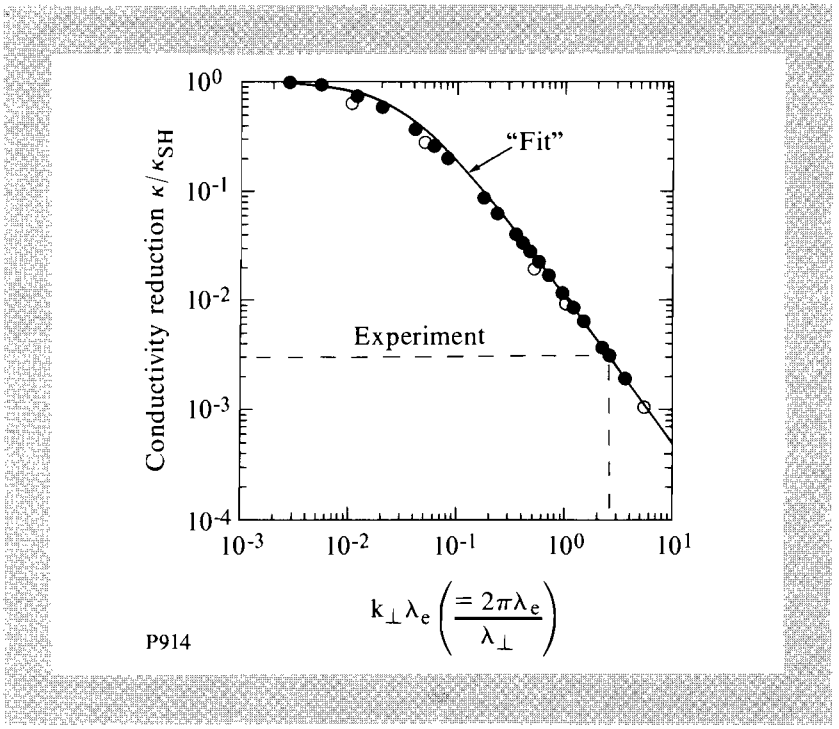

Fig. 49.9
Ratio of the effective conductivity κ to the Spitzer-Härm conductivity κ_{SH} as a function of $k_\perp\lambda_e$, where $k_\perp$ is the perturbation wave number and λ_e is the delocalization length. Solid circles correspond to SPARK results [in the (f_0,f_1) approximation], and the solid curve is a numerical fit to that data. The effect of using higher-order Legendre modes in SPARK is shown by the open circles.

$$f(x,\mathbf{v},t) = f_0(x,v,t) + \mu f_1(x,v,t) + \dots , \tag{1}$$

where μ is the direction cosine. We now define the electron heat flow in the x direction as follows:

$$q(x) = \frac{2\pi m}{3}\int_0^\infty dv\, v^5 f_1(x,v) . \tag{2}$$

In fluid theory, an expression for f_1 can be obtained by assuming small departures from the Maxwellian distribution function f_M and truncating the expansion in Eq. (1) after f_1 (e.g., Ref. 9), i.e.,

$$f_1^{SH}(x,v) = \lambda_s(v)\left(\frac{v^2}{2v_t^2} - 4\right)\frac{1}{T}\frac{\partial T}{\partial x} f_0(x,v), \tag{3}$$

where

$$f_0 = f_M, \lambda_s(v) = v^4 \Big/ \left[4\pi n\left(e^2/m\right)^2 (Z+1)\ln\Lambda\right]$$

is the 90° angular scattering mean free path. [For simplicity, Eq. (3) is given in the high-Z limit.] Substituting Eq. (3) into Eq. (2) yields q_{SH}, and hence κ_{SH}. However, as indicated earlier, nonlocal transport effects can lead to departures from a Maxwellian that invalidate the use of Eq. (3). Using the FP code SPARK, we have calculated the self-consistent f_0 that leads to the modified heat flow. In particular, we have calculated the integrand of the general heat-flow formula [Eq. (2)], i.e., $Q(v) = v^5 f_1$. This has been done for the model heat-flow problem of Fig. 49.9.

Figure 49.10 plots Q(υ) as a function υ/υ_t, for three levels of collisionality: (a) $k_\perp\lambda_e = 0.01$; (b) $k_\perp\lambda_e = 0.05$; and (c) $k_\perp\lambda_e = 0.2$. The dashed curve (which is normalized to unity) is based on f_1^{SH}, using the calculated temperature from the FP code. Since the areas under the curves are proportional to the respective levels of the heat flow, curves (a)–(c) illustrate the effective reduction in the level of heat flow, relative to q_{SH}, as $k_\perp\lambda_e$ increases. These correspond to the values of κ/κ_{SH} in Fig. 49.9.

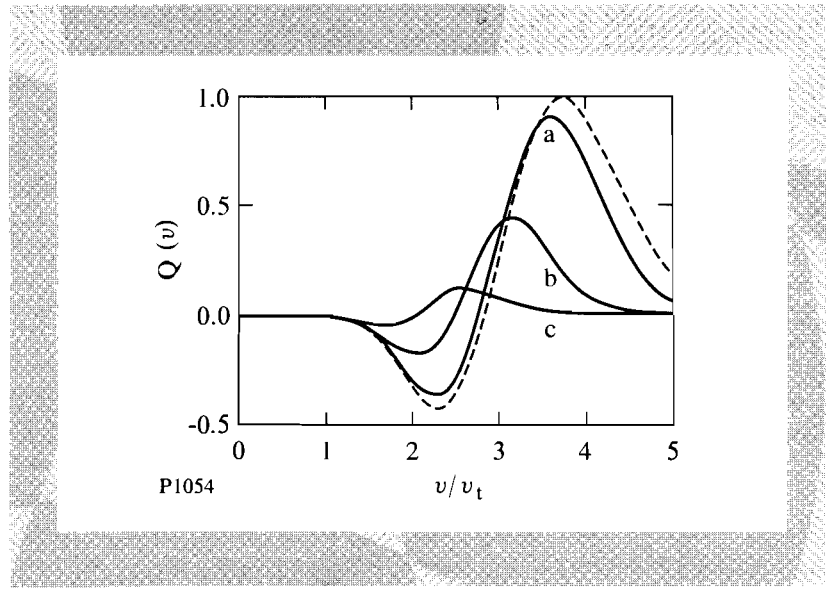

Fig. 49.10
Plot of the heat flux $Q(\upsilon)$, normalized to the corresponding maximum value of $Q_{SH}(\upsilon)$, as a function of υ/υ_t. The dashed curve is the result based on Spitzer-Härm heat flow and the solid curves are obtained from Fokker-Planck simulations for: (a) $k_\perp\lambda_e = 0.01$, (b) $k_\perp\lambda_e = 0.05$, and (c) $k_\perp\lambda_e = 0.2$.

Another important feature of the FP curves is that as the collisionality decreases, i.e., as $k_\perp\lambda_e$ increases, the characteristic velocity υ^* of the main heat-carrying electrons is reduced. Indeed, for $k_\perp\lambda_e = 0.2$ (curve c) $\upsilon^* \approx 2.6\,\upsilon_t$, whereas for the classical collisional case $\upsilon^* \approx 3.7\,\upsilon_t$. So the reduction in the effectiveness of heat flow at short perturbation wavelengths is because the heat is carried mainly by lower velocity electrons, which have higher collision rates.

There are two main approximations in the kinetic treatment of the heat flow adopted in this section. They are the Lorentz approximation (or high-Z) of the collision operator, and the truncation of the Legendre polynomial expansion of the distribution function [i.e., Eq. (1)] after the first two terms.

The first approximation can be partially corrected for by introducing a Z-dependent factor in the angular scattering mean free path λ_s that yields the exact heat-flow coefficient in the strong collisional limit (see Ref. 5). This has some minor implications for the linear theory of filamentation as discussed in the next section.

The second approximation can also be corrected for by appropriately modifying λ_s. To do this we first substitute Eq. (1) into the time-independent electron FP equation (in the Lorentz approximation) and linearize the resultant coupled equations[13] with a harmonic perturbation of the form

$f_0(x,\upsilon) = f_M(\upsilon) + \delta f_0(\upsilon)\exp(ik_\perp x)$, and $f_1(x,\upsilon) = f_1(\upsilon)\exp(ik_\perp x)$, where $l \geq 1$ refers to the Legendre mode, i.e.,

$$\frac{ik_\perp \upsilon}{3} f_1 = C_{ee}(f_M, \delta f_0) + \delta S_{ib}, \tag{4}$$

$$ik_\perp \upsilon \delta f_0 - \frac{e\delta E}{m}\frac{\partial f_M}{\partial \upsilon} + \frac{2}{5} ik_\perp \upsilon f_2 = -\frac{\upsilon}{\lambda_s} f_1, \tag{5}$$

$$\vdots$$

$$\frac{l}{2l-1}(ik_\perp \upsilon f_{l-1}) + \frac{l+1}{2l+3}(ik_\perp \upsilon f_{l+1}) = -\frac{l(l+1)}{2}\frac{\upsilon}{\lambda_s} f_l . \tag{6}$$

Here, δE is the perturbed electric field, C_{ee} is the electron thermalization operator and δS_{ib} is the inverse-bremsstrahlung heating operator.[14] The electron-ion energy exchange is neglected in Eq. (4) since $m << m_i$. After straightforward substitution of Eq. (6) into Eq. (5), it can be shown that the contribution of f_2, f_3, ... into f_1 can be accounted for by defining a new scattering mean free path λ_s^* as follows:

$$\lambda_s^* = \lambda_s \left(1 + \frac{c_2 k_\perp^2 \lambda_s^2}{1 + \frac{c_3 k_\perp^2 \lambda_s^2}{1 + \cdots}} \right)^{-1} \tag{7}$$

where

$$c_l = \frac{4}{(4l^2-1)(l^2-1)} . \tag{8}$$

Such a correction has been introduced into the FP code SPARK and the calculations shown in Fig. 49.9 have been repeated. The new results, displayed as open circles in Fig. 49.9, fall within 10% of the original results. Thus, for the linearized heat-flow problem considered here, it is justifiable to truncate the Legendre polynomial expansion after the first two terms. This conclusion also appears to hold for a variety of heat-flow problems.[11,15]

Analytic Model

The kinetic theory of laser filamentation has been developed in Ref. 4. Here, we review the model and present some improvements with regard to the Z dependence.

The analysis follows the conventional approach of linearizing the electromagnetic wave equation using the slowly-varying-envelope approximation and assuming momentum and energy balance.[2,3] The formula for the spatial growth rate K of the average electric field along its direction of propagation is given by

$$K = \frac{k_\perp}{2\sqrt{\varepsilon}}\left(2\frac{n}{n_c}\left\{\gamma_p + \gamma_T\left(\frac{\kappa_{SH}}{\kappa}\right)\frac{\omega^2}{k_\perp^2 c^2}\right\} - \frac{k_\perp^2 c^2}{\omega^2}\right)^{1/2}, \quad (9)$$

where $k_\perp$ is the perturbation wave number perpendicular to the direction of propagation, c is the speed of light, ω is the laser frequency, n/n_c is the ratio of the electron number density to its critical density and $\varepsilon = (1 - n/n_c)$. Factors γ_p and γ_T, representing ponderomotive and thermal mechanisms, respectively, are defined by

$$\gamma_p = \frac{\text{ponderomotive pressure}}{\text{plasma thermal pressure}} = 9.33 \times 10^{-3} \frac{\lambda_{laser}^2(\mu m) I(10^{14}\,\text{W/cm}^2)}{\sqrt{\varepsilon}(1 + 1/\langle Z\rangle) T(\text{keV})} \quad (10)$$

and

$$\gamma_T = \frac{\text{inverse bremsstrahlung heating rate}}{\text{thermal conduction rate across } (c/\omega)} = 8.95 \times 10^{-9} \frac{I(10^{14}\,\text{W/cm}^2)\left(Z^*\right)^2 (\ln\Lambda)^2}{T^5(\text{keV})\phi\sqrt{\varepsilon}}\left(\frac{n}{n_c}\right)^2, \quad (11)$$

where λ_{laser} is the laser wavelength, T is the background electron temperature (assumed equal to the ion temperature), I is the incident laser intensity, $\langle Z\rangle$ is the average ionization number (where $\langle\ \rangle$ denotes an average over the ion species), $Z^* = \langle Z^2\rangle / \langle Z\rangle$ and $\phi = (Z^* + 0.24)/(1 + 0.24\,Z^*)$. The ratio of the effective thermal conductivity to the classical SH conductivity has been numerically calculated using SPARK, and plotted in Fig. 49.9. An accurate fit to the results is given by

$$\frac{\kappa}{\kappa_{SH}} = \frac{1}{1 + (30 k_\perp \lambda_e)^{4/3}}, \quad (12)$$

where the electron delocalization length is now defined by $\lambda_e = \eta\, T^2/[4\pi n e^4 (Z^* + 1)^{1/2} \ln\Lambda]$, which differs from an earlier definition (Ref. 4), by the factor

$$\eta = \left[\frac{\phi}{4.2}\frac{\left(Z^* + 1\right)}{Z^*}\right]^{1/2} \approx \left[\frac{0.24 + 1.24\left(Z^*\right) + \left(Z^*\right)^2}{4.2\left(Z^*\right) + \left(Z^*\right)^2}\right]^{1/2} \quad (13)$$

This factor provides a correction at low Z (e.g., ionized CH has $Z^* = 5.3$; hence, $\eta = 0.83$) to account for the Lorentz approximation in the original SPARK simulations.

It is apparent from Eq. (9) that a reduction in the effective thermal conductivity relative to its classical value will enhance the thermal filamentation growth rate. Equation (12) shows that this occurs for a perturbation wavelength $\lambda_\perp$ less than some transition value defined by

$$\lambda_c = 60\pi\lambda_e = 3.21 \times 10^3 \frac{T^2(\text{keV})\lambda_{laser}^2(\mu m)}{\ln\Lambda\left(Z^*/\phi\right)^{1/2}}\left(\frac{n_c}{n}\right)\mu m, \quad (14)$$

such that when $\lambda_\perp = \lambda_c$, $\kappa/\kappa_{SH} = 1/2$.

From Eq. (9) it is straightforward to derive the optimum growth rates for thermal and ponderomotive filamentation. These are, respectively,

$$\left(K_{\max}\right)_T^{\mathrm{FP}} = 9.66\times10^{-3}\ \frac{(\ln\Lambda)^{1/2}Z^{*}I^{3/4}(10^{14}\,\mathrm{W/cm^2})}{\varepsilon^{7/8}T^{7/4}(\mathrm{keV})\phi^{1/4}}\left(\frac{n}{n_c}\right)^{5/4}\mu\mathrm{m}^{-1} \quad (15)$$

and

$$\left(K_{\max}\right)_p = 2.93\times10^{-2}\ \frac{\lambda_{\mathrm{laser}}(\mu\mathrm{m})I(10^{14}\,\mathrm{W/cm^2})}{\varepsilon T(\mathrm{keV})(1+1/\langle Z\rangle)}\left(\frac{n}{n_c}\right)\mu\mathrm{m}^{-1} \quad (16)$$

Comparison with the original formulas in Ref. 4 shows slight differences caused by improvements in the Z dependencies currently introduced. These differences are most important for low-Z multi-species plasmas, such as ionized CH, where one should differentiate between $\langle Z\rangle = 3.5$ and $Z^{*} = 5.3$.

SPARK Simulations

In this article SPARK is used as a 2-D Eulerian code, which solves the FP equation for the electrons, the ion fluid equations, and the paraxial wave equation for the laser light. Further details have been described in Refs. 16 and 5.

Here, we investigate the recent filamentation experiment reported by Young (1991),[7] where a 1.06-μm laser beam with a 100-ps FWHM pulse length was intentionally modulated in space and made to interact with a preformed underdense CH plasma. The resulting density perturbations, which are the signature of filamentation, were detected by means of a short-pulse (<100 ps) probe beam and were estimated to reach about 3%.

The conditions of the background plasma are assumed to be equivalent to those reported by Young *et al.* (1988) from a LASNEX simulation.[6] Following the same prescription used in Ref. 5 we consider a homogeneous temperature of 0.8 keV, and a uniform density in the x-y plane with a parabolic density profile in the z direction approximated by

$$\frac{n}{n_c} = 0.25\left[1-0.6\left(\frac{z}{400}\right)^2\right], \quad (17)$$

where the density varies from 0.25 n_c at $z = 0$, to 0.1 n_c at $z = \pm400$ μm. The interaction beam is modeled by $I(x, t) = I_0(t)(1 + 0.68\cos k_{\perp}x)$, where $\lambda_{\perp} = 40$ μm, and $I(x = 0, t = 0) = 5\times10^{13}$ W/cm^2. The time dependence of $I_0(t)$ is modeled by a Gaussian with a 100-ps FWHM.

In view of the symmetry of the problem, the simulation is restricted to $0 \le x \le \lambda_{\perp}/2$, with reflective boundary conditions imposed at $x = 0$ and $\lambda_{\perp}/2$. Zero heat flow is likewise imposed at the $z = \pm400$-μm boundaries, though free plasma flow is allowed there.

Figure 49.11 shows the surface plot of the normalized laser intensity I/I_0 in the x-z plane at the peak of the pulse (i.e., at $t = 0$ ps). (To illustrate the

periodicity of the problem the plots are extended to $1.5 \times \lambda_{\perp}$ along x.) The large intensity amplification observed in the FP simulation is principally caused by thermal self-focusing, whereas the small amount of amplification observed in the SH simulation is because of ponderomotive self-focusing only (the plasma is stable to classical thermal filamentation). The dominance of the so-called kinetic thermal mechanism over the ponderomotive one has been previously predicted by analytic theory[4] and by FP simulations under similar conditions.[5] and is a direct consequence of a reduction in heat conductivity, as discussed previously.

To compare with experiment it is more useful to calculate the density modulation $\delta n/n_0$, where n_0 is the average number density along x. Figure 49.12 plots $\delta n/n_0$, in terms of percentage values, for both FP and SH simulations at $t = 0$ ps. We observe from the figure that the density modulations predicted by the FP simulation are not only about ten times higher than those predicted by the SH simulation, but are also consistent with the 3% density-modulation value measured experimentally.

Implications to ICF

The simulation presented in the previous section serves to illustrate the physics of laser filamentation and provides a valuable comparison with experimental results. There are, however, important differences between these and the conditions relevant to ICF. In the first place, the plasma in ICF targets is not homogeneous, but has time-varying density gradients and flow. It has been shown, for example, that plasma flow perpendicular to the direction of laser propagation can either enhance or reduce the filamentation level, depending on whether it is subsonic or supersonic, respectively.[17] More important, however, is the fact that the laser irradiation can have a large spectrum of time-varying spatial modes.

Modern schemes for improving laser irradiation uniformity often involve some combination of phase plates,[18] which create a high-frequency speckle pattern in the target plane, and smoothing by spectral dispersion (SSD)[19] or induced spatial incoherence (ISI),[20] which introduce a temporal variation to the speckle pattern. The basic philosophy behind these schemes is that the high-frequency spatial modulation in the laser-energy deposition will be smoothed out by heat conduction in the plasma atmosphere. Further smoothing is then achieved, provided that the time variation in the speckle pattern is shorter than the characteristic hydrodynamic time scale of the plasma. Indeed, Schmitt has shown, by means of a 3-D filamentation code with linearized hydrodynamics and classical heat transport, that ISI or SSD can completely eliminate filamentation.[21] Unfortunately, the use of classical thermal conductivity in his simulations has led to an underestimate of the level of thermal filamentation.[22]

However, rather than perform filamentation simulations for specific types of laser irradiation profiles, we will restrict ourselves to the estimation of filamentation growth lengths L_g for some laser-target systems of current interest for direct-drive ICF, such as the 30-kJ OMEGA Upgrade system (currently under construction) and a hypothetical 5.9-MJ Laboratory Microfusion Facility (LMF). The plasma parameters are derived from hydrodynamic code simulations of CH spherical shells irradiated by 350-nm laser light.[23] They are

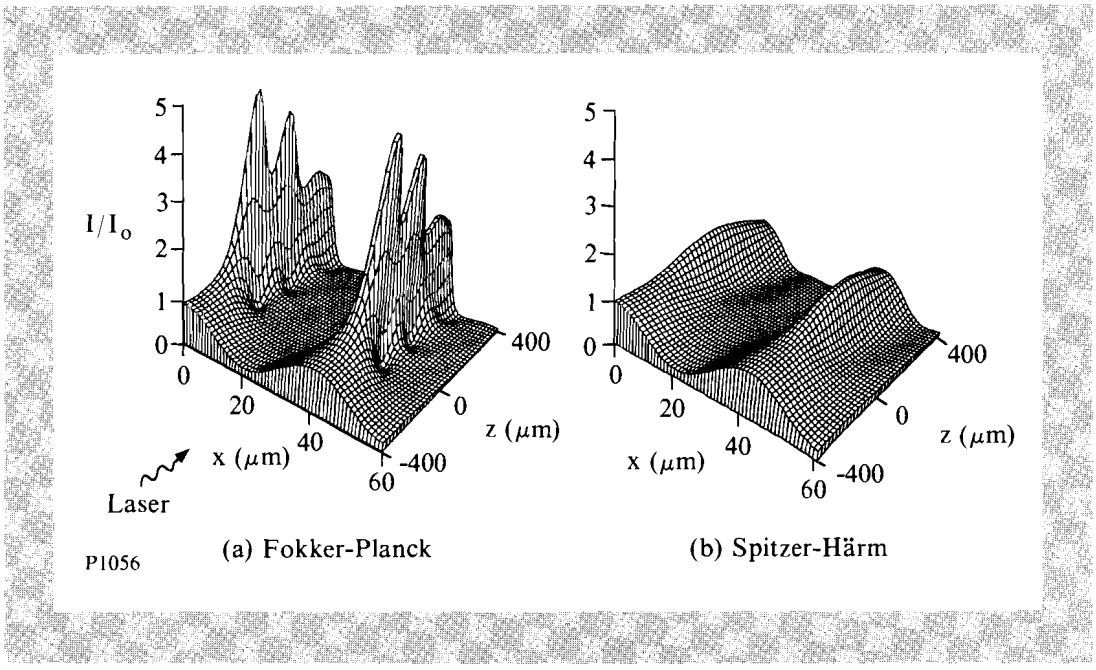

Fig. 49.11
Surface plots of the normalized laser intensity I/I_o on the x-z plane at $t = 0$ ps (i.e., at the peak of the laser pulse), for (a) Fokker-Planck transport and (b) Spitzer-Härm transport.

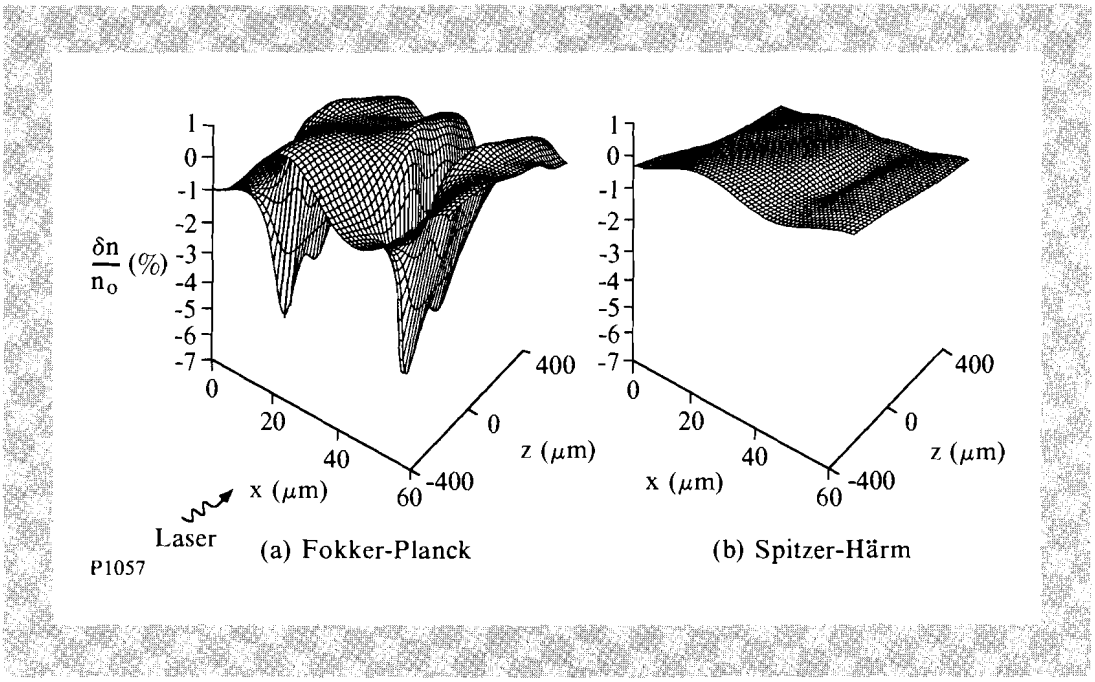

Fig. 49.12
Surface plots of normalized density modulation $\delta n/n_o$ on the x-z plane at $t = 0$ ps, for (a) Fokker-Planck transport and (b) Spitzer-Härm transport.

representative of plasma conditions at 0.1 n_c at peak laser intensity (quoted as a single-beam intensity).

The intensity filamentation growth length, which is related to the spatial growth rate by $L_g = (2K)^{-1}$, is calculated using Eq. (9) and plotted in Figs. 49.13 and 49.14 as a function of $\lambda_\perp$. The different solid curves correspond to the various filamentation mechanisms [i.e., kinetic thermal, ponderomotive and thermal (with $\kappa = \kappa_{SH}$)]. The horizontal lines indicate the density scale length L_n, and laser attenuation length L_{ib} (based on collisional absorption).

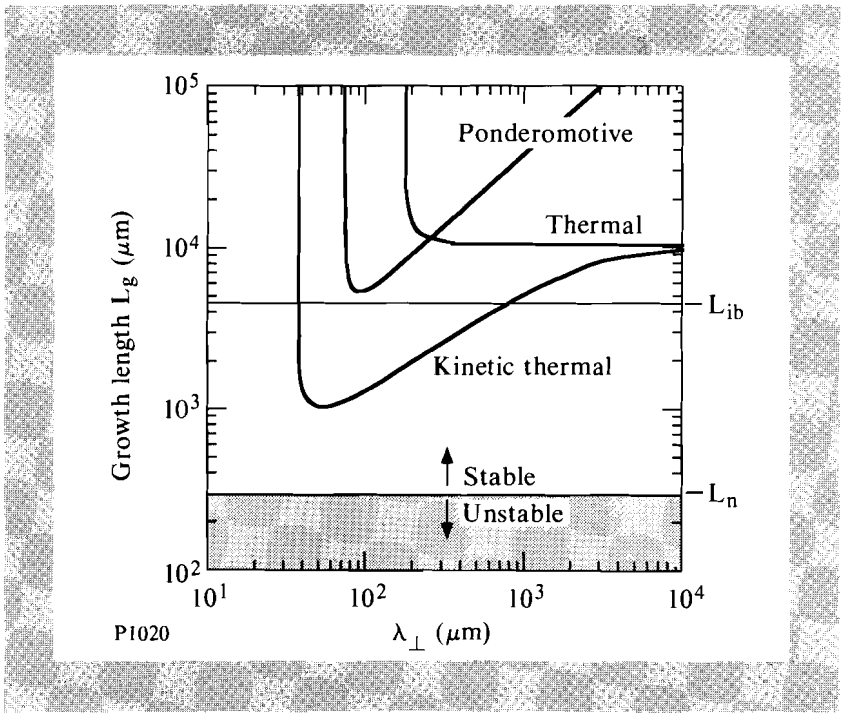

Fig. 49.13
Plot of the filamentation growth length (in microns) as a function of perturbation wavelength $\lambda_\perp$ (in microns) at the simulated plasma conditions expected for the OMEGA Upgrade [30 kJ, $\langle Z \rangle = 3.5$, $n/n_c = 0.1$, $T = 2.75$ keV, $I_0 = 3.2 \times 10^{13}$ W/cm^2 (single beam), and $\lambda_L = 0.35$ μm] for three models of filamentation. If the growth length exceeds the plasma density scale length L_n (as is the case here for all models) the plasma is considered to be stable to filamentation.

If we adopt the criterion for significant filamentation as $L_g < \min(L_n, L_{ib})$,[1] it is clear that (at least for the given plasma conditions) the proposed direct-drive ICF schemes appear not to be susceptible to filamentation. This filamentation criterion is based on linear homogeneous theory and, as such, does not take into account the possibility of stabilization through SSD or ISI schemes as previously discussed. Neither does it take into account the potential destabilizing effects of hot spots in the laser beam. Nevertheless, we believe that it provides a useful guideline for the likelihood of generating filaments.

In order to generalize our results to other plasma conditions we have also derived approximate formulas for the optimum growth lengths $L_{g,}$, by simplifying Eqs. (15) and (16) (assuming $\ln\Lambda = 8$),

$$\left(L_g\right)_T^{FP} \approx 24 \frac{T^{1.8}(\text{keV})}{Z^* I^{0.8}(10^{14}\,\text{W/cm}^2)\left(\frac{n}{n_c}\right)^{1.3}}\,\mu\text{m}, \tag{18}$$

and

$$\left(L_g\right)_P \approx 17 \frac{T(\text{keV})}{\lambda_{\text{laser}}(\mu\text{m})\, I(10^{14}\,\text{W/cm}^2)\left(\frac{n}{n_c}\right)} \mu\text{m} . \tag{19}$$

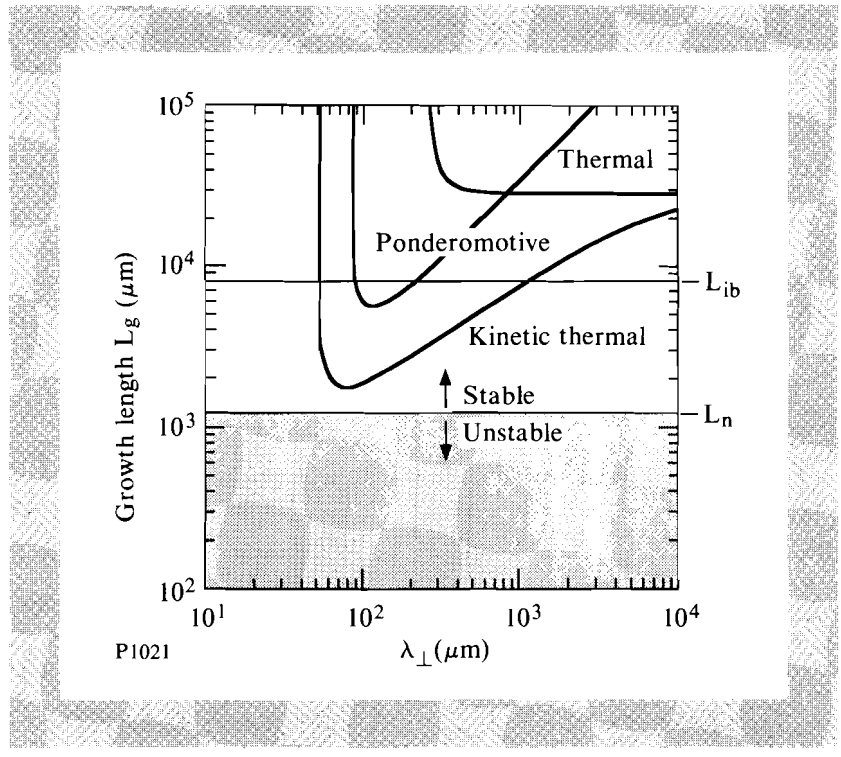

Fig. 49.14
Plot of the filamentation growth length (in microns) as a function of perturbation wavelength $\lambda_\perp$ (in microns) at the simulated plasma conditions expected for a direct-drive LMF system [5.9 MJ, $\langle Z \rangle$ = 3.5, n/n_c = 0.1, T = 4.5 keV, $I_o = 4.35 \times 10^{13}$ W/cm^2 (single beam), and λ_L = 0.35 μm].

Conclusions

We have reviewed the nature of nonlocal heat transport and shown that plasmas with arbitrarily small temperature modulations of wavelength less than about 200 electron mean free paths can experience a significant reduction in the thermal conductivity as compared with classical Spitzer-Härm theory. The reduction in the effectiveness of the heat conduction has been demonstrated to be caused by a shift of heat-carrying electrons to lower velocities. Such nonlocal transport effects have been shown to be accurately modeled by expanding the electron distribution function into the first two Legendre modes only.

The effect of nonlocal electron heat transport on the linear stability theory of laser filamentation has been reviewed with some improvements for low-Z and multi-species plasmas. Simulations with the 2-D FP code SPARK reproduce well the density modulations observed in a filamentation experiment reported by Young. These results confirm the prediction of analytic theory that the main mechanism driving the filamentation of the laser is kinetic thermal rather than ponderomotive. Simple estimates of filamentation growth lengths, based on the linear homogeneous kinetic theory, have shown that for current direct-drive ICF systems, the single-beam intensities are below the threshold for filamentation.

ACKNOWLEDGMENT

We thank Dr. R. S. Craxton, Dr. J. Delettrez, Dr. R. Epstein, Dr. A. Simon, and Dr. C. P. Verdon for many useful discussions. This work was supported by the U.S. Department of Energy Office of Inertial Confinement Fusion under agreement No. DE-FC03-85DP40200 and by the Laser Fusion Feasibility Project at the Laboratory for Laser Energetics, which is sponsored by the New York State Energy Research and Development Authority and the University of Rochester.

REFERENCES

1. W. L. Kruer, Comments Plasma Phys. & Controlled Fusion **9**, 63 (1985); P. E. Young, Comments Plasma Phys. & Controlled Fusion **12**, 53 (1988); W. L. Kruer, Phys. Fluids B **3**, 2356 (1991); and W. Seka, Bull. Am. Phys. Soc. **36**, 2375 (1991).
2. P. Kaw, G. Schmidt, and T. Wilcox, Phys. Fluids **16**, 1522 (1973).
3. M. S. Sodha, A. K. Ghatak, and V. K. Tripathi, in *Progress in Optics*, edited by E. Wolf (North Holland, Amsterdam, 1976), Vol. 13, p. 169; J. N. McMullin, C. E. Capjack, and C. R. James, Comput. Phys. Commun. **23**, 31 (1981).
4. E. M. Epperlein, Phys. Rev. Lett. **65**, 2145 (1990).
5. E. M. Epperlein, Phys. Fluids B **3**, 3082 (1991).
6. P. E. Young *et al.*, Phys. Rev. Lett. **61**, 2336 (1988).
7. P. E. Young, Phys. Fluids B **3**, 2331 (1991).
8. D. R. Gray and J. D. Kilkenny, Plasma Phys. **22**, 81 (1980); A. R. Bell, R. G. Evans and D. J. Nicholas, Phys. Rev. Lett. **46**, 243 (1981); J. Delettrez, Can. J. Phys. **64**, 932 (1986) and references therein.
9. L. Spitzer, Jr. and R. Härm, Phys. Rev. **89**, 977 (1953).
10. R. C. Malone, R. L. McCrory, and R. L. Morse, Phys. Rev. Lett. **34**, 721 (1975).
11. A. R. Bell, Phys. Fluids **26**, 279 (1983).
12. E. M. Epperlein and R. W. Short, Phys. Fluids B **3**, 3092 (1991); E. M Epperlein, *Research Trends in Physics: Nonlinear and Relativistic Effects in Plasmas*, edited by V. Stefan (American Institute of Physics, New York, 1991) p. 43; LLE Review **42**, 57 (1990).
13. I. P. Shkarofsky, T. W. Johnston, and M. A. Bachynsky, *The Particle Kinetics of Plasmas* (Addison-Wesley, London, 1966); T. W. Johnston, J. Math. Phys. **7**, 1453 (1966).
14. A. B. Langdon, Phys. Rev. Lett. **44**, 575 (1980).
15. J. P. Matte and J. Virmont, Phys. Rev. Lett. **49**, 1936 (1982); J. P. Matte, T. W. Johnston, J. Delettrez, and R. L. McCrory, Phys. Rev. Lett. **53**, 1461 (1984); J. F. Luciani, P. Mora, and R. Pellat, Phys. Fluids **28**, 835 (1985).
16. E. M. Epperlein, G. J. Rickard, and A. R. Bell, Phys. Rev. Lett. **61**, 2453 (1988); E. M. Epperlein, G. J. Rickard, and A. R. Bell, Comput. Phys. Commun. **52**, 7 (1988); G. J. Rickard, A. R. Bell, and E. M. Epperlein, Phys. Rev. Lett. **62**, 2687 (1989).

17. R. W. Short, R. Bingham, and E. A. Williams, Phys. Fluids **25**, 2302 (1982).

18. Y. Kato *et al.*, Phys. Rev. Lett. **53**, 1057 (1984).

19. S. Skupsky, R. W. Short, T. Kessler, R. S. Craxton, S. Letzring, and J. M. Soures, J. Appl. Phys. **66**, 3456 (1989).

20. R. H. Lehmberg and S. P. Obenschain, Opt. Commun. **46**, 27 (1983).

21. A. J. Schmitt, Phys. Fluids B **3**, 186 (1990).

22. A. J. Schmitt, Bull. Am. Phys. Soc. **36**, 2335 (1991).

23. C. P. Verdon (private communication).

Section 2
ADVANCED TECHNOLOGY DEVELOPMENTS

2.A Microstructural Control of Thin-Film Thermal Conductivity

Modeling of thin-film systems with absorbing inclusions[1] has indicated that thermal conductivity may play a role in laser damage of such films. Several studies have shown conclusively that thermal conductivity values for thin films are often lowered,[2–3] sometimes by an order of magnitude, from the thermal conductivity of corresponding bulk materials.

While mechanisms of thermal resistance have been well-characterized for bulk materials both theoretically and experimentally,[4] it is unclear which defects play primary roles in thin-film systems. Thermal-resistance mechanisms can be roughly divided into two categories; those for which the material may be treated as a continuum (voids, second phases), and those for which we must consider atomic-scale interactions in order to accurately predict thermal properties.

In this article, we seek to identify which thermal-resistance mechanisms are responsible for lowering thin-film thermal conductivity. To do this, measurements of the thin-film thermal conductivities for four systems are made, and the results interpreted in terms of the observed thin-film microstructures. Depending upon the film system studied, we use continuum and/or atomic-scale theoretical models to help illustrate which thermal-resistance mechanisms are at work.

While continuum thermal-conductivity-reduction mechanisms are easily understood and often straightforwardly modeled, by a rule of mixtures or a series of resistors, for example,[5] atomic-scale interactions require a more complicated

theoretical treatment. To simplify, we can assume that the primary heat carriers in a solid at room temperature are lattice vibrations (phonons), and charge carriers such as electrons. For a metal, both are important, while for a dielectric, like most of the materials used in thin-film optics, the primary contribution to heat conduction is from phonons. It is often convenient to treat phonons as particles encountering various scattering events as they propagate through a solid, leading to momentum loss or thermal resistance. We can express thermal conductivity K quite simply as

$$K = \frac{1}{3} C v l \,, \tag{1}$$

where C is the specific heat, v the velocity, and l the mean free path of the phonons. Equation (1) suggests clearly the effect of reducing the mean free path of phonons, or other heat carriers, on thermal-conductivity depression.

Expressions equivalent to Eq. (1) have been derived for thermal conductivity based on relaxation time,[6] or time between heat carrier-scattering events $\tau(x)$:

$$K = \frac{k_B}{2\pi^2 v}\left(\frac{k_B T}{\hbar}\right)^3 \int_0^{\Theta_D/T} \tau(x) \frac{x^4 e^x}{\left(e^x - 1\right)^2} dx \,, \tag{2}$$

where k_B = Boltzmann's constant, $\hbar$ = Planck's constant/2π, T is the absolute temperature, Θ_D is the Debye temperature, and v is the phonon or acoustic wave velocity. The term x is defined

$$x = \frac{\hbar\omega}{k_B T} \,, \tag{3}$$

where ω is the phonon frequency. In turn, relationships have been developed that predict the effects of various defects on the relaxation time $\tau(x)$ and hence the thermal conductivity.[7–8] These theoretical relationships have been experimentally confirmed for many cases, including grain boundary and point-defect scattering.[9–10] In any event, evidence shows that a very small fraction of impurities or other defects can substantially lower thermal conductivity, both theoretically and experimentally.

We review data and microstructures for four thin-film systems; rare earth-transition metals (RE-TM), ZrO_2, $YBa_2Cu_3O_{7-\delta}$, and AlN. Each film is important in a specific application requiring dissipation of heat or knowledge of thermal transport: RE-TM for magneto-optical recording, ZrO_2 for optical-interference coatings, $YBa_2Cu_3O_{7-\delta}$ for superconducting microelectronics, and AlN for microelectronics and optics.

Experimental Techniques

Thermal conductivity of thin films is a difficult quantity to measure, and many techniques have been attempted. Here, we use the thermal-comparator technique, described in detail by Lambropoulos[2] *et al.* The thermal conductivity of a film/substrate system is measured by detecting the temperature drop of a metal probe brought into contact with the front face of the film, and comparing it to temperature drops recorded when the probe is in contact with materials of known

thermal conductivity. The substrate effect is removed via a solution of the heat-conduction equation for a thin film on a semi-infinite substrate, leaving a quantity K_{eff}, the thermal conductivity of the film including the effect of the film/substrate interfacial thermal resistance. The interfacial thermal resistance R_{int} can also be eliminated by measuring several thicknesses and treating the system as resistors in series, so that

$$\frac{t}{K_{\text{eff}}} = \frac{t}{K_f} + R_{\text{int}} \ , \tag{4}$$

where t is the film thickness and K_f is the quantity of interest, the thermal conductivity of the film itself. Furthermore. by plotting t/K_{eff} versus t, as in Fig. 49.15, we obtain K_f from the inverse of the slope. The thermal conductivity of a thin film measured in this way is actually the thermal conductivity perpendicular to the plane of the film, since the dimension of the probe is much larger than that of the film thickness.

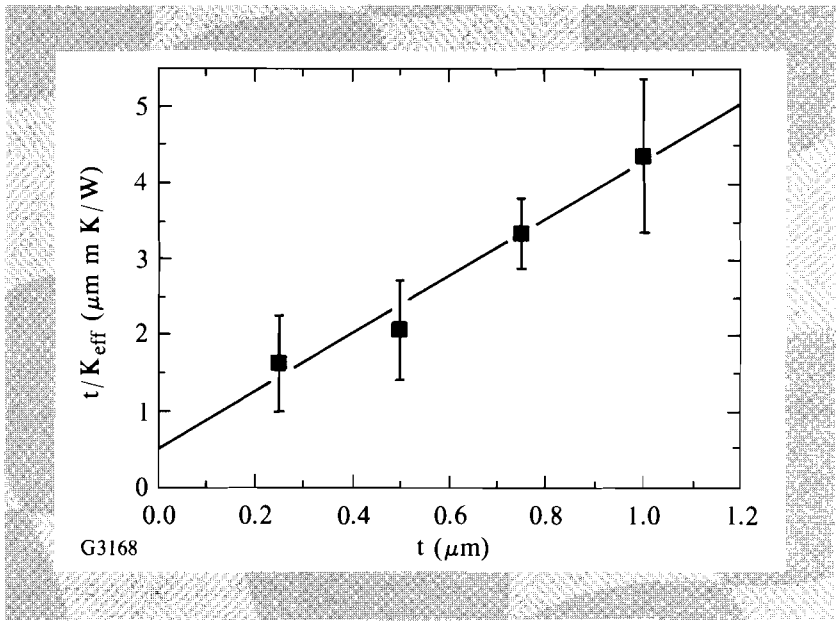

Fig. 49.15
Plot of Eq. (4) for a well-behaved system ($YBa_2Cu_3O_{7-\delta}$). 1/slope = film thermal conductivity K_f.

In the cases of the RE-TM and the $YBa_2Cu_3O_{7-\delta}$ films, it is also possible to measure the thermal conductivity in the plane of the film by using the Wiedemann-Franz-Lorenz conversion. Following the technique of Anderson,[11] the electrical sheet conductivity is measured directly by the four-point probe method, and converted via the Lorenz ratio to the electronic contribution to the thermal conductivity. The remaining contribution to the thermal conductivity, caused by phonon transport, is then estimated based on previous work and added to the electronic contribution to obtain a measure of K_f, this time in the plane of the film.

In order to determine the primary thermal-resistance mechanisms at work in each film system, the films were carefully characterized by a variety of techniques, including scanning electron microscopy (SEM), transmission electron microscopy (TEM), x-ray diffraction (XRD), infrared transmission spectroscopy (IR), x-ray photoelectron spectroscopy (XPS), and Rutherford backscattering (RBS).

The preparation conditions for each film material varied, and are mentioned in the discussion of each system.

RE-TM Films—Effect of Columnar Structure

A series of amorphous rare earth-transition metal (TbFeCoZr) films was sputtered from a single homogeneous target onto fused quartz substrates. In order to duplicate the variations in columnar morphology typically observed for metal films sputtered at various pressures,[12] the films were sputtered at three different pressures; 2 mTorr, 7 mTorr, and 15 mTorr.

Thermal conductivity was measured through the plane of the films ($K_{\perp}$) using the comparator technique, and in the plane of the films ($K_{||}$) using the Wiedemann-Franz conversion technique described previously.[13] The values for $K_{\perp}$ and $K_{||}$ are shown in Table 49.I for the three pressures. Noticeable trends are that $K_{||}$ is generally smaller than $K_{\perp}$, and that it is significantly lower for the film deposited at the highest pressure.

Table 49.I: Thermal conductivity of RE-TM films.

Deposition Pressure (mTorr)	$K_{\perp}$ (W/mK)	$K_{||}$ (W/mK)
2	7.0	5.0
7	7.3	4.4
15	4.3	0.3

G3224

While the thermal conductivity of such a material in bulk form has never been reported, the thermal conductivity of a similar metallic glass FeNiCr has been calculated based on an estimate of the carrier mean free path as the interatomic distance. This projected value for bulk amorphous FeNiCr is 10 W/mK. The values for $K_{\perp}$ reported here are not much less than this, while the values for $K_{||}$ are slightly reduced for the cases of 2- and 7-mTorr, and significantly reduced for the case of 15-mTorr deposition.

An explanation for the observed behavior is shown in the SEM micrographs of the film cross sections in Figs. 49.16–49.18. Note that as expected, the films become more columnar as deposition pressure is increased. Since the columns are oriented perpendicular to the film surfaces, heat can flow directly down the columns for the measurement of $K_{\perp}$, but must encounter internal intercolumnar contacts during the measurement of $K_{||}$. The films are amorphous and the mean free paths of the heat carriers are on the order of the interatomic spacing, which is much less than the intercolumnar distance. Therefore, the concept of phonon or electron scatter is not particularly useful in describing the intercolumnar thermal resistance. Instead, we can treat the films as a continuum containing sources of internal resistance arranged in series in the film planes. From such a treatment, we can estimate the intercolumnar thermal contact resistance

$$\frac{w}{K_{\parallel}} = \frac{w}{K_{\perp}} + R_{\text{col}} \ , \tag{5}$$

where w is the column diameter, from Fig. 49.18 about 0.15 μm, and R_{col} is the intercolumnar contact resistance, which calculated from Eq. (5) is 4.7×10^{-7} m^{2}K/W. This is a very low thermal resistance compared with typical values for metal surfaces in contact,[14] indicating that there is little trapped gas (indicative of porosity) or other impurity content between the columns, which was confirmed by RBS. So, even very clean, dense films can have their thermal conductivities severely compromised, especially in the plane of the films, through the introduction of a columnar microstructure.

While we have investigated sputtered metal films, the same anisotropy should be observed for other sputtered films including dielectrics, as well as for evaporated and chemical-vapor-deposited films, which both typically show evidence of columnar or dendritic growth features.[15–16]

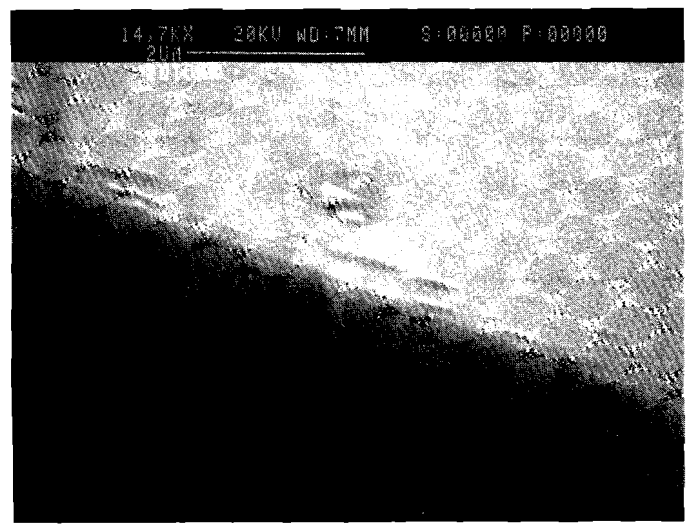

G3169

Fig. 49.16
SEM of TbFeCoZr cross section deposited at 2 mTorr.

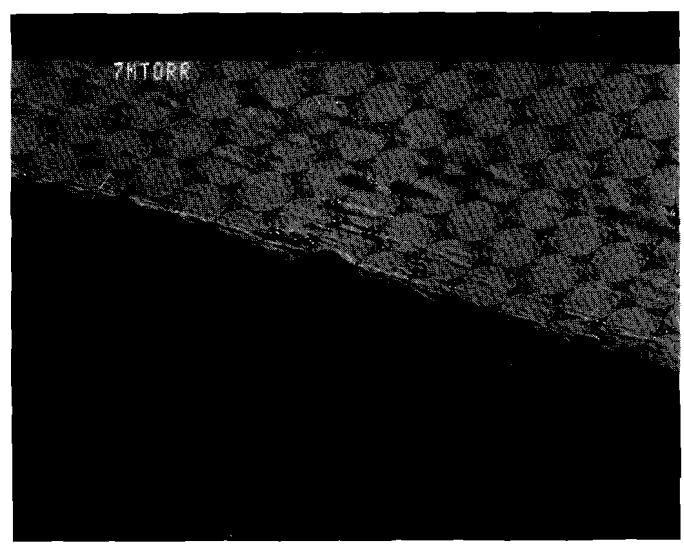

G3170

Fig. 49.17
SEM of TbFeCoZr cross section deposited at 7 mTorr.

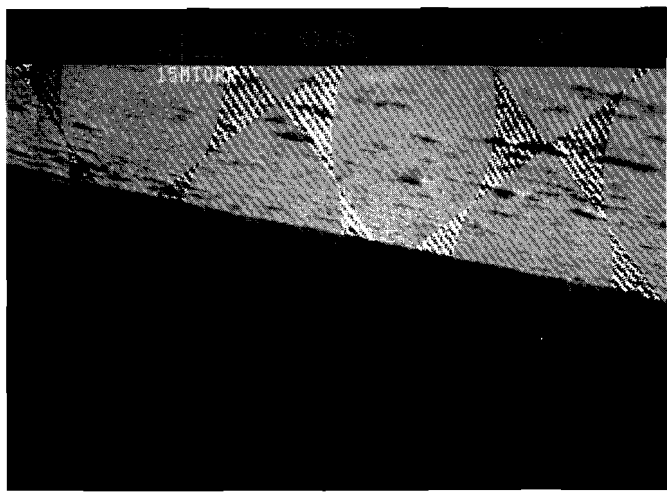

Fig. 49.18
SEM of TbFeCoZr cross section deposited at 15 mTorr.

G3171

ZrO_2—The Effect Of Variation in Crystal Structure

ZrO_2 films were *e*-beam evaporated from ceramic targets onto polished silicon, single-crystal (111)-oriented substrates. During deposition, the substrates were heated to 300°C.

The thermal-comparator method was used to obtain the thin-film thermal conductivity perpendicular to the plane of the films. The derivation of K_{eff}, the thermal conductivity of the film and film/substrate interface, yielded very unusual results. Figure 49.19 shows the plot of Eq. (4), which is generally used to extract the thermal conductivity of the film material. Comparison with the well-behaved plot in Fig. 49.15 shows the anomalous behavior inherent in the ZrO_2 films. Since all four thicknesses studied were deposited identically onto similar substrates, it is unlikely that the film/substrate interfacial resistance is varying. Therefore we conclude that the thermal conductivity of the thinner films is far too low compared with that of the thicker films. This renders it impossible to fit a positive slope to the data, making it impossible to extract a single reasonable value for the thin-film thermal conductivity.

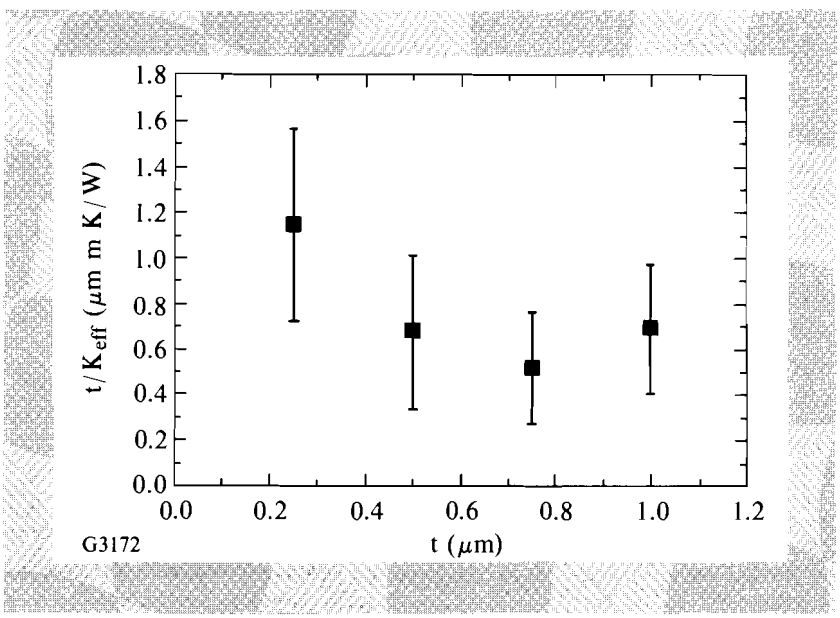

Fig. 49.19
Plot of Eq. (4) for *e*-beam-evaporated ZrO_2. Compare with behavior shown in Fig. 49.15.

To find the source of this anomaly, the microstructure of the evaporated films was investigated. Figure 49.20 shows a TEM of a cross section of a ZrO_2 film. The film has a crack associated with the sample preparation, but more relevant is the fact that film is denser near the substrate (bottom of the micrograph) and becomes more obliquely columnar near the free surface. This situation would predict a higher thermal conductivity for the material nearer the substrate (the denser region), which is counter to the measurements of K_{eff}. Another possible source for the observed values of K_{eff} is the change in crystal structure with thickness often observed for ZrO_2 films.[17]

The three common polymorphs of ZrO_2 exhibit different thermal conductivities,[18] shown in Table 49.II. Most interesting is the value for cubic ZrO_2, a factor of two lower than the others. While transmission electron diffraction did not distinguish clearly the crystal structure of various regions of the films, IR spectroscopy shows the variation of crystal structure through the films. Figure 49.21 shows the transmission IR scans for each of four regions of a 1-μm-thick film taken for the frequency range 800–200 cm^{-1}. Each curve represents only 2500 Å of film material, and by comparing absorption peaks with previous data,[19] we can determine the crystal structure of each portion of the film. The 2500 Å curve shows a rather featureless region, indicating a large quantity of amorphous material, while the 5000 Å curve shows the emergence of some cubic material. The cubic material fades away and is replaced by monoclinic material for the two curves representing the regions of the films closest to the free surface.

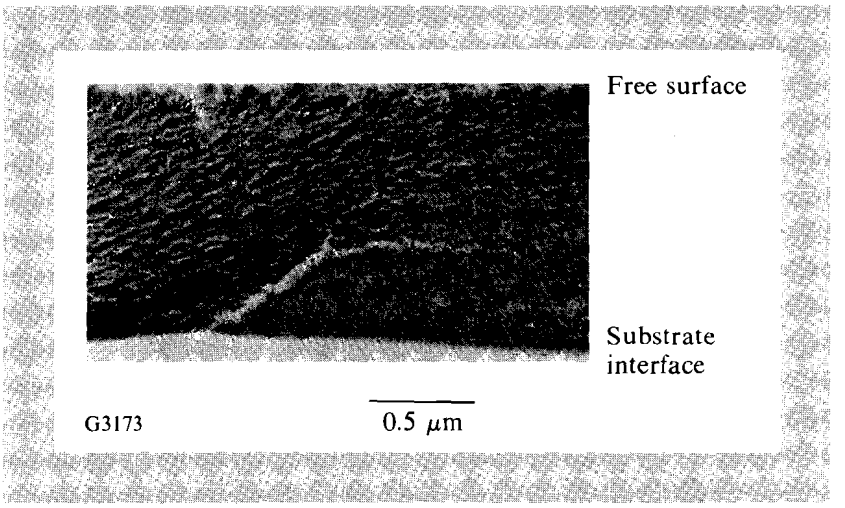

Fig. 49.20
TEM of ZrO_2 film cross section.

We conclude that the films are becoming less cubic and more monoclinic as deposition proceeds, and that an amorphous phase is present, especially near the substrate surface. Since amorphous materials typically show thermal conductivities suppressed by an order of magnitude from their crystalline counterparts;[20] the thinner films, consisting of cubic and amorphous material, are naturally poorer conductors of heat than the thicker films, containing the monoclinic phase.

Annealing is often used to crystallize and stabilize ZrO_2 films, with the added attraction that the thermal conductivity should also increase. Future work will include annealing of the ZrO_2 films to determine the effect on thermal conductivity and microstructure.

Table 49.II: Thermal conductivity of ZrO_2 polymorphs.[18]

Crystal Structure	Thermal Conductivity (W/mK)
cubic	1.8
tetragonal	4.8
monoclinic	5.2

G3225

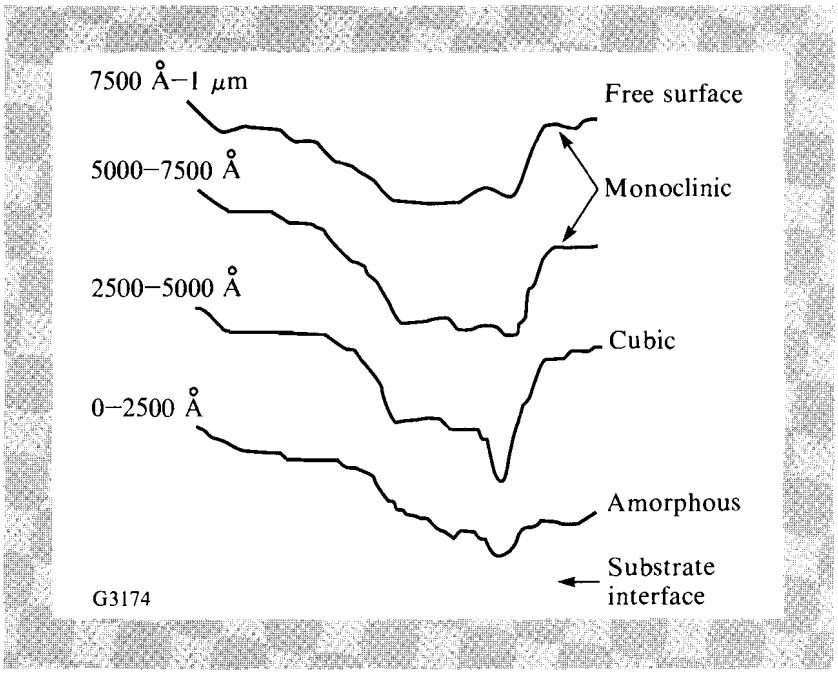

Fig. 49.21
Transmission IR scans for portions of evaporated ZrO_2 film. Each segment is 2500 Å, with the bottom curve corresponding to the film segment closest to the substrate.

$YBa_2Cu_3O_{7-\delta}$—Intrinsic Anisotropy and Hillock Growth

$YBa_2Cu_3O_{7-\delta}$, a ceramic, high-temperature superconductor, has been extensively studied in single-crystal platelet form. Most device applications now under development, including fast switches[21] and integrated circuits,[22] require that the material be in thin-film form. Knowledge of the thin-film thermal conductivity is important in predicting device stability.[23]

Thermal-conductivity measurements on $YBa_2Cu_3O_{7-\delta}$ single crystals have shown that thermal conductivity is anisotropic, and arises from different carrier combinations depending on crystal orientation.[24]

In the *a-b*, or superconducting planes, the thermal conductivity at room temperature typically varies from 8–12 W/mK, with 45% of the heat transport supplied by phonons and the remainder by electrons. Along the *c* axis, the thermal conductivity ranges from 1–2 W/mK with 95% of the heat carried by phonons. Another important effect is the oxygen content, or value of δ, which is directly related to the superconducting transition temperature.[25]

This factor accounts for some of the variation within a given direction, mentioned previously. Other defects do not affect the thermal conductivity of this material significantly at room temperature,[26] since the phonon mean free path is sufficiently small that defects such as stacking faults, twins, or grain boundaries would have to be much more closely spaced than is commonly observed in order to have a significant effect.

The films studied here were sputtered[27] from a ceramic source onto single-crystal (100) MgO substrates held at 730°C. XRD indicated that the films were oriented with the *c* axis perpendicular to the plane of the films. The thermal-comparator method yielded a thermal-conductivity value of 0.26 W/mK, which because of the film orientation must be a *c*-axis value. The Wiedemann-Franz-Lorenz conversion resulted in in-plane, or *a-b* plane values enumerated in Table 49.III.

Table 49.III: Thermal conductivity and superconducting transition temperatures for $YBa_2Cu_3O_{7-\delta}$ films.

Thickness (Å)	$K_{\perp}$, W/mK (comparator)	$K_{\parallel}$, W/mK (W-F-L)	T_c, K
2500		4.4	77
5000		4.5	83
7500	0.26	2.4	87
10,000		2.9	84

G3226

In both directions, the thermal conductivity is significantly depressed from the single-crystal values, but the anisotropy present in the single-crystal material is preserved in the thin films, with a slightly greater reduction observed perpendicular to the plane of the films. The values of the superconducting transition temperatures indicate that the films are close to stoichiometric, in fact that δ is around 0.2. Therefore, lack of stoichiometry is not a primary source of thermal resistance in the films.

The SEM cross section in Fig. 49.22 reveals a more likely reason for the lower thermal-conductivity values of the films. The very distinct hillocks on the film surface were analyzed by energy-dispersive spectroscopy, and showed higher barium and copper content than occurred in the film proper. The yttrium content is about the same, and the relative oxygen content could not be analyzed. The hillock material is, therefore, a distinct phase from the rest of the film, likely rich in $BaCuO_2$ and possibly CuO_2, and hence a probable source for lowered thermal conductivity.

Many other materials show anisotropic thermal-conductivity behavior in single-crystal form, which would be expected to exist in oriented thin-film form as well. Some examples include[28–29] rutile TiO_2 (K_a = 5.5 W/mK,

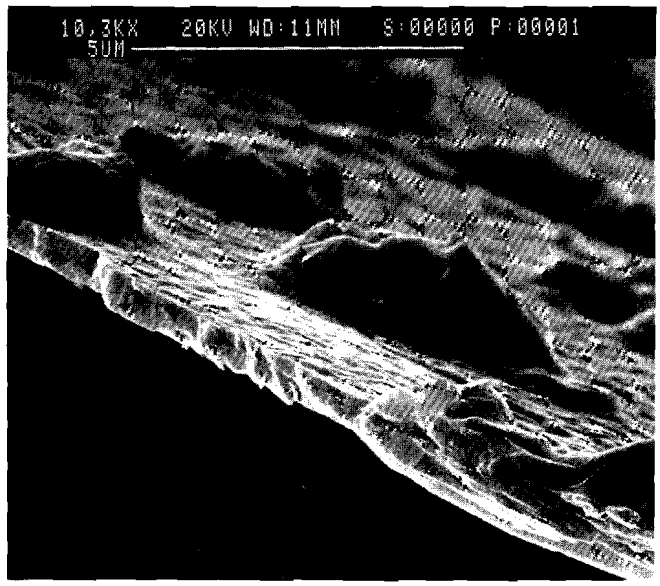

G3175

Fig. 49.22
SEM of $YBa_2Cu_3O_{7-\delta}$ cross section showing hillocks on film surface.

$K_c = 7.6$ W/mK), quartz SiO_2 ($K_a = 4.5$ W/mK, $K_c = 8.7$ W/mK), and graphite ($K_a = 355$ W/mK, $K_c = 89$ W/mK). Also, the phase separation, which resulted in hillock formation in this case, is often observed during thin-film deposition of superconducting ceramics of other compositions.[30]

AlN—The Effect of Phonon Mean-Free-Path-Scale Scattering

AlN in single-crystal form exhibits a very high room-temperature thermal conductivity[31] of 320 W/mK. Since the phonons, the primary heat carriers in AlN, have a very long mean free path, study of this material provides a good opportunity for illustration of phonon-scattering events as sources of thermal resistance.

AlN was sputtered from a ceramic target onto glass substrates. When measured perpendicular to the plane of the film using the thermal comparator, the thermal conductivity of the film was 16 W/mK.[32] This decrease of more than an order of magnitude from the bulk value is drastic, but has been confirmed in previous measurements for AlN films.[33,34]

One common source of thermal resistance in AlN is the presence of vacancies that must form to conserve charge upon the introduction of oxygen impurities. A very small addition of oxygen is theoretically predicted to cause a large drop in the thermal conductivity. This effect can be calculated using the following expression for time between phonon scattering events $\tau(x)$:

$$\tau^{-1}(x) = \frac{x^4 k_B^4 T^4}{4\hbar^4 \pi v^3} f(1-f)\left[\left(\frac{\Delta M}{M}\right)^2 + \epsilon\left(\frac{\Delta\delta}{\delta}\right)^2\right], \qquad (6)$$

where variables are defined as for Eq. (2), with $\Delta M/M$ the fractional change in mass caused by the impurity introduction, $\Delta\delta/\delta$ the strain change, ϵ an empirical constant, and f the impurity atom fraction. Note that for vacancies, the term

$\Delta M/M$ is large, and substitution of Eq. (6) into Eq. (2) predicts a large drop in thermal conductivity, which is shown graphically in Fig. 49.23. XPS showed that the films studied here contain about 1-at.-% oxygen impurity, which accounts for a decrease in thermal conductivity of 50%. This is, therefore, a significant source of phonon scatter and thermal-conductivity reduction.

We must also consider the interruption of phonons by interaction with internal boundaries, such as grain boundaries, and external boundaries, such as the film surfaces. In this case, τ may be expressed

$$\tau^{-1} = v / d \, . \tag{7}$$

If this expression is substituted into Eq. (2), we obtain the dependence of thermal conductivity on grain size or film thickness for AlN, shown in Fig. 49.24.

Figure 49.25 shows a plan view of a typical AlN film. Note that the very small grain size of 30 nm may be expected to significantly contribute to thermal resistance through grain boundary scattering. However, the TEM cross-sectional micrograph shown in Fig. 49.26 shows that the grains extend through the thickness of the film. Since the comparator measures thermal conductivity in that direction, it is unlikely that the mean free paths of the phonons in question are interrupted by "bouncing" off grain boundaries as they travel perpendicular to the film plane.

More likely to cause phonon scatter are the upper and lower surfaces of the film. In fact, at room temperature, theory predicts a reduction in thermal conductivity for boundary scattering shown in Fig. 49.24. For boundaries separated by 1 μm, thermal conductivity is reduced at room temperature by 20%, and an even greater reduction occurs for thinner films.

Another important feature of the thin film cross section of Fig. 49.26 is that near the substrate, there is an apparently disordered region. Assuming that this disorder is an amorphous, near-substrate region often associated with thin-film deposition, a rather pronounced effect would be expected on $K_\perp$. This is because perpendicular to the film plane

$$\frac{t}{K_\perp} = \frac{t_a}{K_a} + \frac{t_c}{K_c} \, , \tag{8}$$

where t is the film thickness, t_a is the thickness of the disordered region, t_c is the thickness of the crystalline region, K_a is the thermal conductivity of the amorphous material, and K_c is the thermal conductivity of the crystalline region. If we assume that the thermal conductivity of the amorphous region is about an order of magnitude lower than that of the crystalline region,[20] and from Fig. 49.25 that the amorphous region takes up about 20% of the total thickness, then Eq. (8) predicts that the introduction of the disordered region near the substrate reduces $K_\perp$ an additional 64%.

Finally, with all nanocrystalline materials, we must consider the amorphous nature and the volume fraction of material occupied by grain boundaries. The

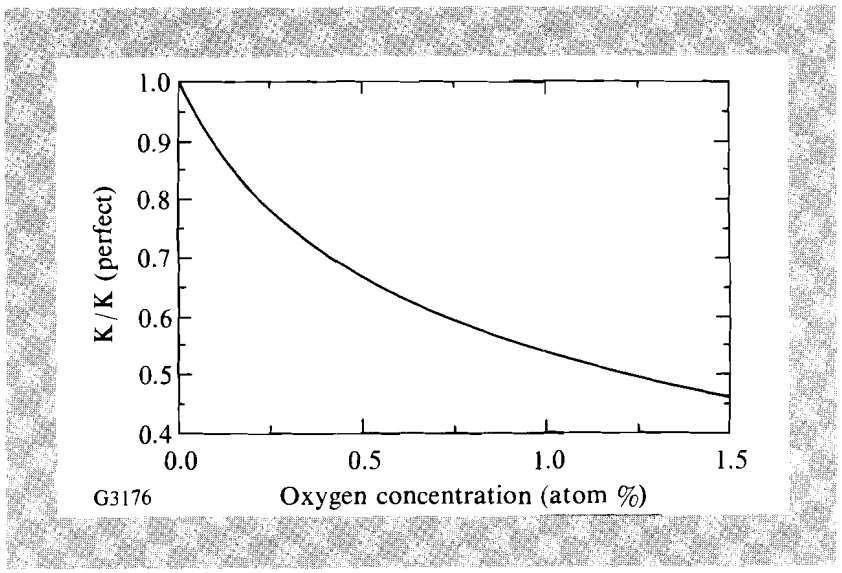

Fig. 49.23
Theoretical dependence of AlN thermal conductivity on oxygen content, calculated from Eqs. (6) and (2).

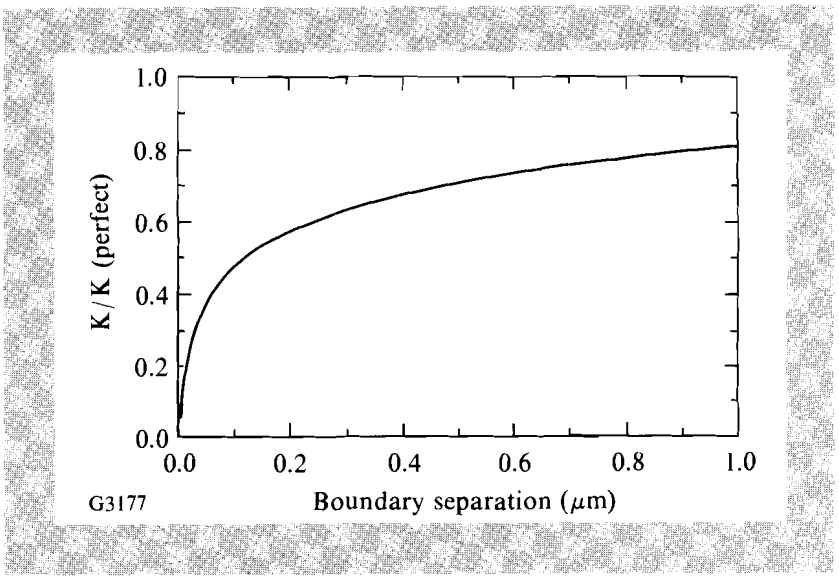

Fig. 49.24
Theoretical dependence of AlN thermal conductivity on interface separation (e.g., grain size or film thickness), calculated from Eqs. (7) and (2).

grain boundaries in Fig. 49.25 appear white because no diffraction of the electron beam has occurred, i.e., they are amorphous. This is consistent with models[35] for nanocrystalline microstructures, and of interest is the volume fraction of material that these amorphous regions occupy. Since amorphous materials have much lower thermal conductivity than crystalline materials (because of the reduction of the phonon mean free path to approximately the interatomic spacing), any material containing a significant volume fraction of amorphous regions should show a drop in thermal conductivity. Perpendicular to the plane of the film, these amorphous regions would have parallel heat paths and would lower the conductivity as resistors in parallel:

$$K_{\perp} = V_a K_a + V_c K_c \ , \tag{9}$$

where V_a and V_c are the volume fractions occupied by the amorphous (grain boundary) regions and the crystalline regions, respectively. In a material with a

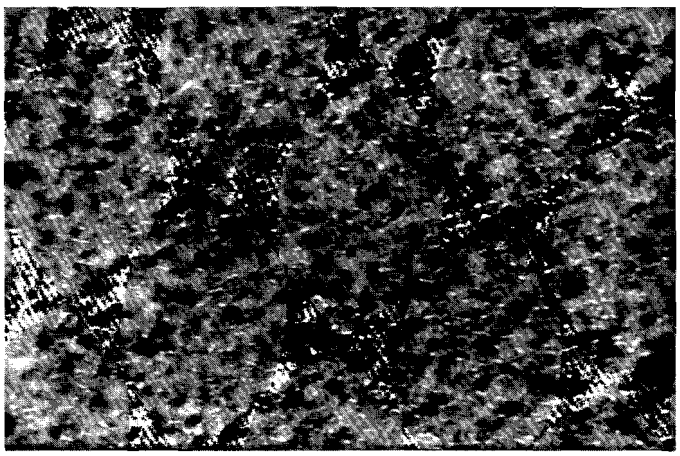

Fig. 49.25
Plan view TEM of sputtered AlN film.

G3178

Fig. 49.26
TEM of sputtered AlN, showing a cross section of the film.

G3179

grain size of 1–10 nm, the amorphous grain boundaries occupy 50% of the volume.[35] If we conservatively estimate that for the AlN films the grain boundaries occupy 10% of the volume, Eq. (9) predicts a decrease in thermal conductivity of about 9%.

If we consider all of the thermal-resistance sources identified for AlN, we can account for an expected thermal conductivity of about 50 W/mK, still higher than the observed value. One likely source of the lower measured value is a probable overestimate for K_a, the thermal conductivity of amorphous AlN. Because no data based on actual measurements is available, we have estimated an order-of-magnitude reduction from the crystalline form based on SiO_2 data.[20] However, for a material with a high Debye temperature such as AlN ($\Theta_D = 950$ K), at room temperature, the difference between the amorphous and crystalline values of thermal conductivity is likely to be more than an order of magnitude.[36] Some additional unaccounted for thermal-resistance sources may also be responsible, such as undetected impurities.

So, for AlN, we have identified several contributions to thermal resistance, including impurities, a dimensional (thickness) effect, the disordered interfacial region, and the nanocrystalline microstructure. Except for the thickness effect, these factors may be controlled during deposition of the films.

Other film systems for which the mechanisms discussed for AlN are expected to be important include those with long phonon and/or electron mean free paths, such as crystalline metals and covalent ceramics including SiC, Al_2O_3, and diamond.

Summary

Experimental results and suggestions for increasing thermal conductivity for each of the systems studied here are shown in Table 49.IV. In general, we have found that

(1) Primary mechanisms of thermal resistance in thin films vary depending upon film material and deposition conditions.

   (a) Columnar microstructure introduces a strong thermal-conductivity anisotropy caused by the introduction of intercolumnar contacts.

   (b) Changes in crystal structure during thin-film deposition can introduce uncertainty in extracting thermal-conductivity values.

   (c) Intrinsic thermal-conductivity anisotropy carries over to thin-film form if the films are highly oriented.

   (d) Hillock growth of a second phase reduces thermal conductivity.

   (e) For materials with long heat-carrier mean free paths, (usually characterized by high Debye temperatures and high intrinsic thermal conductivities), many microstructural defects contribute strongly to thermal resistance, particularly point defects and 2-D boundaries.

   (f) Because they possess a heat-carrier mean free path on the order of the interatomic distance, amorphous materials or materials with amorphous regions always exhibit thermal-conductivity values significantly lower than their crystalline counterparts.

(2) Thermal conductivity of thin films can be optimized by identifying important system parameters and adjusting film-deposition conditions. The resulting improved conductivity should aid the goal of improving laser-damage resistance.

ACKNOWLEDGMENT

This work was supported by the U.S. Department of Energy Office of Inertial Confinement Fusion under agreement No. DE-FC03-85DP40200 and by the Laser Fusion Feasibility Project at the Laboratory for Laser Energetics, which is sponsored by the New York State Energy Research and Development Authority and the University of Rochester. This work was also supported by Texaco.

The following persons were also very helpful in the preparation of this work: M. Jin and R. Chrzan of the Laboratory for Laser Energetics, B. McIntyre of The Institute of Optics, Professor A. Kadin and D. Mallory of the Department of Electrical Engineering, and T. K. Hatwar, A. Palumbo, and D. Glocker of the Eastman Kodak Company.

Table 49.IV: Summary of results.

Film Material	K_{film} (W/mK)	Thermal-Resistance Mechanisms	Suggested Remedy
RE-TM	4.3–7.3 ($K_{\perp}$) 0.3–5.0 ($K_{\|\|}$)	intercolumnar contacts	increase deposition temperature, decrease deposition pressure
ZrO_2	? (anomalous)	crystal-structure variations	anneal to obtain monoclinic or tetragonal phase
$YBa_2Cu_3O_{7-\delta}$	0.26 ($K_{\perp}$) 2.4–4.5 ($K_{\|\|}$)	intrinsic anisotropy, hillock growth	reduce hillocks by encouraging equilibrium growth
AlN	16	impurities, thickness effect, disorder at interface, amorphous grain boundaries	improve vacuum cleanliness, heat substrate, increase grain size

G3227

REFERENCES

1. A. H. Guenther and J. K. McIver, Thin Solid Films **163**, 203 (1988).
2. J. C. Lambropoulos, M. R. Jolly, C. A. Amsden, S. E. Gilman, M. J. Sinicropi, D. Diakomihalis, and S. D. Jacobs, J. Appl. Phys. **66**, 4230 (1989).
3. D. L. Decker, L. G. Koshigoe, and E. J. Ashley, in *Laser Induced Damage in Optical Materials: 1984, Natl. Bur. Stand. (U.S.), Spec. Publ. 727* (Government Printing Office, Washington, DC, 1986), pp. 291-297.
4. P. G. Klemens, in *Solid State Physics*, edited by F. Seitz and D. Turnbull, *Advances in Research and Applications, Vol. 7* (Academic Press, New York, 1958), pp. 1–98.
5. W. D. Kingery, H. K. Bowen, and D. R. Uhlmann, in *Introduction to Ceramics, 2nd ed.* (Wiley, New York, 1976), pp. 634–643.
6. J. Callaway, Phys. Rev. **113**, 1046 (1959).
7. P. G. Klemens, Proc. Phys. Soc. LXVIII **12-A**, 1113 (1955).
8. P. G. Klemens, Can. J. Phys. **35**, 441 (1957).
9. R. B. Dinwiddie and D. G. Onn, in *Advanced Electronic Packaging of Materials*, edited by A. F. Barfknecht, J. P. Partridge, C. J. Chen, and C.-Y. Li (Materials Research Society, Pittsburgh, PA, 1990), Vol. 167, pp. 241–246.
10. R. K. Williams *et al.*, J. Appl. Phys. **62**, 2778 (1987).

11. R. J. Anderson, J. Appl. Phys. **67**, 6914 (1990).

12. J. A. Thornton, in *Modeling of Optical Thin Films* (SPIE, Bellingham, WA, 1987), Vol. 821, pp. 95–103.

13. L. J. Shaw-Klein, T. K. Hatwar, S. J. Burns, S. D. Jacobs, and J. C. Lambropoulos, J. Mater. Res. **7** (to be published).

14. R. W. Heimburg and K. N. Tong, in *Thermal Conductivity, Proceedings of the Eighth Conference*, edited by C. Y. Ho and R. E. Taylor (Plenum Press, New York, 1969), pp. 527–540.

15. A. G. Dirks and H. J. Leamy, Thin Solid Films **47**, 219 (1977).

16. D. T. Morelli, C. P. Beetz, and T. A. Perry, J. Appl. Phys. **64**, 3063 (1988).

17. E. N. Farabaugh *et al.*, J. Vac. Sci. Technol. A **5**, 1671 (1987).

18. D. P. H. Hasselman *et al.*, Am. Ceram. Soc. Bull. **66**, 799 (1987).

19. C. M. Phillippi and K. S. Mazdiyasni, J. Am. Ceram. Soc. **54**, 254 (1971).

20. W. D. Kingery, H. K. Bowen, and D. R. Uhlmann, in *Introduction to Ceramics, 2nd ed.* (Wiley, New York, 1976), p. 625.

21. W. R. Donaldson, A. M. Kadin, P. H. Ballentine, and R. Sobolewski, Appl. Phys. Lett. **54**, 2470 (1989).

22. R. Simon, Phys. Today, June 1991, 64.

23. M. I. Flik and C. L. Tien, *Annual Review of Heat Transfer*, edited by C. L. Tien (Hemisphere Publishing Corp., New York, 1990), Vol. 3, pp. 115–144.

24. S. T. Hagen, Z. Z. Wang, and N. P. Ong, Phys. Rev. B **40**, 9389 (1989).

25. R. J. Cava *et al.*, Physica C **165**, 419 (1990).

26. R. K. Williams *et al.*, J. Appl. Phys. **66**, 6181 (1989).

27. P. H. Ballentine *et al.*, J. Vac. Sci. Technol. A **9**, 1118 (1991).

28. *CRC Handbook of Chemistry and Physics, 51st ed.*, edited by R. C. Weast (The Chemical Rubber Company, Cleveland, OH, 1970), p. E-5.

29. J. F. Nye, *Physical Properties of Crystals* (Clarendon Press, Oxford, 1964) p. 196.

30. T. N. Blanton, C. L. Barnes, and M. Lelental, Physica C **173**, 152 (1991).

31. G. A. Slack *et al.*, J. Phys. Chem. Solids **48**, 641 (1987).

32. L. J. Shaw-Klein, S. J. Burns, and S. D. Jacobs, in *Electronic Packaging Materials Science V*, edited by E. D. Lillie, P. S. Ho, R. Jaccodine, and K. Jackson (Materials Research Society, Pittsburgh, PA, 1991), Vol. 203, pp. 235–240.

33. D. Raasch and S. Klahn, J. Magn. & Magn. Mater. **93**, 365 (1991).

34. R. P. Tye (private communication).

35. R. Birringer and H. Gleiter, in *Encyclopedia of Materials Science and Engineering*, edited by R. W. Cahn (Pergamon Press, Oxford, 1988), Suppl. Vol. 1, pp. 339–349.

36. D. G. Cahill and R. O. Pohl, Ann. Rev. Phys. Chem. **39**, 93 (1988).

2.B Energy Transport in a Modern Disk Amplifier

The University of Rochester's Laboratory for Laser Energetics has designed, built, and characterized a modern, 20-cm clear aperture, Nd:glass Brewster-disk amplifier. This device will be used as the final amplifier in the upgrade of the existing OMEGA laser system. This article describes results of the energy characterization of that amplifier. Specifically, spatially resolved measurements of small-signal gain and whole-beam measurements of large-signal gain are described. The amplifier met its small-signal-gain design goal of 3.0 at only 70% of the design capacitor-bank energy with adequate spatial uniformity. A storage efficiency of 1.7% was achieved. Large-signal-gain measurements, both with and without 5-Å-FM bandwidth on the extracting beam, display no measurable change in gain because of the impressed bandwidth.

The amplifier is termed modern in that it incorporates a number of improvements suggested by others in the community[1] who have extensive experience in building disk amplifiers, as well as several uniquely new features. A few examples of these improvements include minimization[2] of total amplifier volume for better coupling of flash lamps to laser glass, transversely-pumped rectangular design to avoid obscuration of flash lamps by the disk supports,[3] water-cooled flash lamps,[4] and polymerically-bonded edge cladding.[5]

A brief description of the amplifier follows; the detailed design and construction of the amplifier is described elsewhere.[6,7] A picture of the amplifier with some of its flash lamps removed for clarity is shown in Fig. 49.27. The amplifier consists of four disks of 2-wt% Nd:phosphate glass, 3.0 cm thick. The number of disks was chosen in order to obtain adequate gain at the 3.0-cm thickness. The 3.0-cm thickness and the 550-μs $3\sqrt{LC}$ pump pulse width are optimized for high-gain-per-unit path in glass in order to minimize B-integral. The disks rest on edge, that is, their surface normals lie in a horizontal plane. The amplifier is pumped by 80, 19-mm bore, 10-in. arc length, vertically oriented (transverse), xenon flash lamps. The lamps are mounted on 1.341-in. centers for a packing fraction of 1.75. These lamps are connected in series of five, both electrically and for cooling. Each group (brick) of five lamps is connected to one pulse-forming network (PFN) that can deliver 18.8 kJ of energy at 100% of nominal bank energy. At this bank energy the lamps operate at 26% explosion fraction.

G3250

Fig. 49.27
Picture of the 20-cm-disk amplifier with the near-side flash-lamp modules lowered for clarity. Note the transversely mounted flash lamps.

The characterization of this amplifier proceeded in two phases: energy transport and wavefront. Energy-transport measurements were performed first to determine if the amplifier met design goals for gain and extraction. After it was verified that the amplifier met energy goals, the wavefront was characterized using time-resolved Mach-Zehnder interferometry. Wavefront results will be presented at a later date. Energy-transport measurements included passive loss, small-signal gain, and large-signal gain. Small-signal-gain measurements were made as a function of position in the clear aperture and bank energy to obtain information about the internal dynamics of the amplifier. The large-signal-gain tests were conducted with the anticipated spectral bandwidth for the OMEGA Upgrade because of recent reports[8] of reduced extraction at large incoherent (~25 Å) bandwidths.

Small-Signal Gain

The small-signal gain was measured with the apparatus[9] shown in Fig. 49.28. This apparatus measured the small-signal gain at three locations on a diameter of the aperture (either horizontal or vertical) simultaneously, thus reducing the number of shots required. Typically, the inner beam measured the center-line gain, while the two outer beams were translated across the diameter. A polarized cw Nd:YLF oscillator operating on the 1.054-μm transition was collimated, expanded to a 1-cm diam, and split three ways. Each of the three beams was then injected into the amplifier. A mirror with a small horizontal tilt (<1 mrad) returned the beams back through the amplifier. The small offset (<0.4 cm) between the input and return of the beams on the first disk did not significantly affect the spatial resolution of the measurement. Each return beam was first dispersed by a grating to discriminate against spectrally-near fluorescence. Each beam then reflected from a 1-μm mirror to limit the amount of flash-lamp light reaching the detector. Spatial filters with a 1-mrad full-angle cutoff followed the

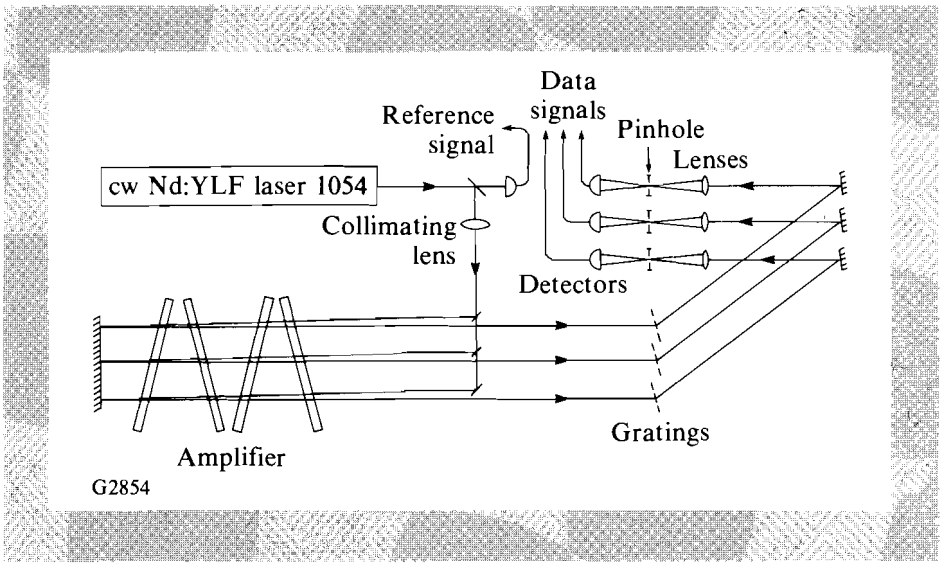

Fig. 49.28
Schematic of the small-signal-gain apparatus. The cw Nd:YLF laser is split into three beams that probe different locations on either a horizontal or vertical diameter in the aperture. The return signals are filtered spectrally with gratings and spatially filtered before detection.

mirrors. Large-area photodiodes with a measured 1/e response time of 2 μs detected the return signals. A fourth identical photodiode monitored the Nd:YLF laser output as a reference channel.

Signals from the large-area photodiodes were digitized by Tektronix[10] 2440 oscilloscopes with a 500-megasample-per-second, maximum-digitizing rate. Signals were digitized into 2-ms, 1024-sample record lengths with 8-bit amplitude resolution. The 2-ms record length ensured that the entire temporal history of the gain and a portion of all signals prior to the initiation of the flash-lamp discharge were recorded. The signals were then Fourier transformed, filtered with a Blackman[11] filter whose cutoff frequency was 100 kHz. Background "shots" were taken at intervals during the measurement. For these shots, the cavity of the Nd:YLF was blocked and all of the signals mentioned previously were recorded. This background included fluorescence from the amplifier and any noncancelling noise. It was determined that the fluorescence part of the signal from the amplifier was negligible and only a DC offset from the detectors was significant. The background offset collected for each channel was subtracted from the data for that channel. The temporal variations of the Nd:YLF were removed by dividing each of the three signal channels by the reference channel. A 200-μs sample of each of the three channels prior to the initiation of the discharge was averaged and set equal to unity gain. The remainder of the data in that channel was multiplied by the so-determined constant to convert the data to gross small-signal gain. The peak gain in the channel was picked with a simple search routine. The estimated precision attained as a result of this procedure is ±1%. A 90-mm-rod amplifier with dedicated pump modules (flash lamps) and diagnosed power conditioning was kept as a control. The gain of this amplifier could be routinely remeasured with ±1% precision.

Initial measurements were of center-line gain versus capacitor-bank energy. The results are plotted in Fig. 49.29. The design goal of 3.0 was achieved at 70% of nominal bank energy. This corresponds to a disk-thickness-averaged, stored-

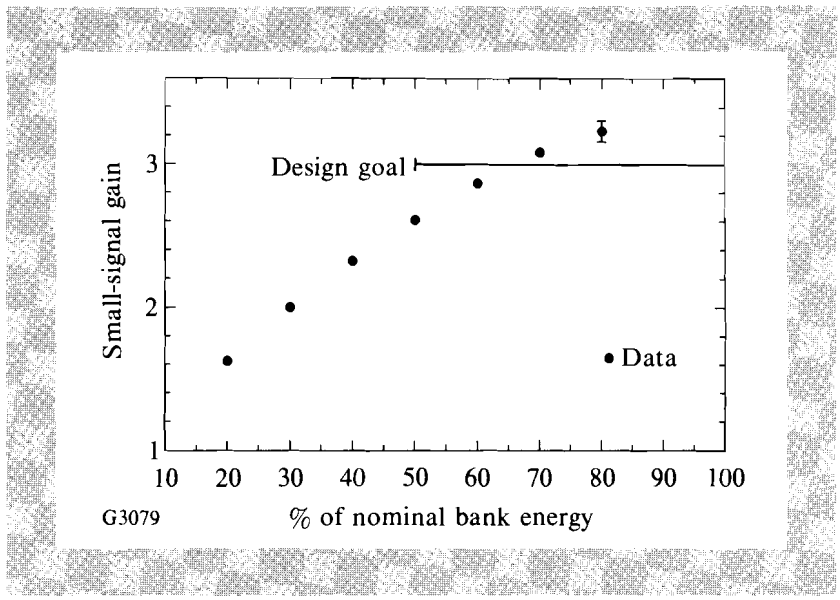

Fig. 49.29
Measured small-signal gain versus the percentage of nominal capacitor-bank energy. The small-signal design goal was achieved at 70% of the design bank energy.

energy density of 0.41 J/cc assuming a stimulated-emission cross section of 3.5×10^{-20} cm^2. The data displays no sharp rollover or plateau that would signify parasitic clamping or severe amplified spontaneous emission (ASE) limiting.[12]

The fact that the gain design goal was achieved at only 70% of "nominal" bank energy provides a margin of safety for both power balance[13] and, more importantly, long-term amplifier performance. Equalization of individual amplifier gains will be necessary in order to maintain instantaneous power balance among the OMEGA Upgrade beamlines. It is a well-known observation that amplifier performance declines with number of shots. Causes of this degradation include effects such as solarization of the laser glass, blast windows, water jackets, etc., reflector tarnishing, and damage caused by inadequate cleanliness in the pump cavity. Simulations show that a 25% reduction in the gain of the amplifier results from a 15% reduction in the reflectivity in the pump cavity. The extra gain margin ensures that this amplifier will perform to specification near end of life (20,000 shots). For all further testing the amplifier was operated just over its gain design goal at 80% of nominal bank. This corresponded to a center-line small-signal gain of 3.22±0.03. This was done to ensure that had any short-term gain decrease occurred, the testing would have been carried out at at least the design gain. The corresponding $\alpha_o \overline{E}_s D$ product for these disks is 2.93 where $\overline{E}_s = 0.44$ J/cm^3 and D is the major diameter of the 20-cm clear aperture projected at Brewster's angle.

The small-signal gain was next measured as a function of position on the horizontal and vertical diameters of the aperture. In order to separate the effects of shot-to-shot gain variations from actual spatial variations, the inner probe beam monitored the center-line gain while only the outer two probe beams were translated along the diameters. Outer probe-beam data from different shots were normalized by comparing the center-line gains. The shot-to-shot variation in the center-line gain was small, amounting to ±1.5%, 3σ over the course of these measurements.

The results are shown plotted in Fig. 49.30. Note the ~20% decline in gain as the "minus" side of the aperture is approached on the horizontal diameter. Note also the ~3% increase in gain on the "plus" side of the amplifier. This is the well-known "cold-side" effect[14] that is characteristic of disk amplifiers having an even number of disks. This effect can be summarized as follows: The two end disks are not evenly pumped across the horizontal axis. The edges of the disks closest to the entrance and exit apertures of the amplifier have only a small solid angle subtended by unfiltered flash lamps and are thus relatively weakly pumped. In an amplifier with an even number of disks, these weakly pumped or "cold" portions of the end disks are both on the same side of the amplifier and therefore add.

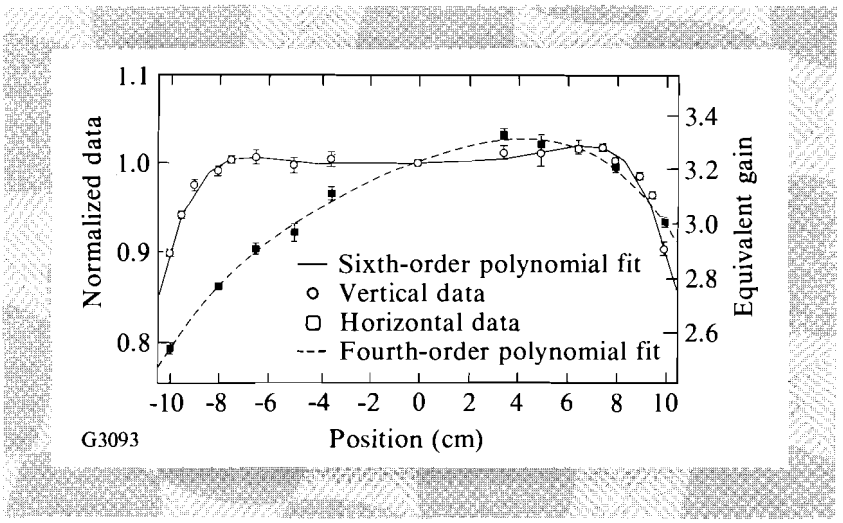

Fig. 49.30
Measured small-signal gain on a horizontal and vertical diameter.

The gain-uniformity goal was ±10% of the center-line gain at any location in the clear aperture. The original center-line gain goal was 3.0. Thus, the goal was to have the gain at any location within the clear aperture be between 2.7 and 3.3. By operating the amplifier at a center-line gain of 3.22, it can be seen from Fig. 49.30 that the small-signal gain at any location within the aperture is in the range of 2.57 to 3.32. Improvements to the gain uniformity, particularly near the edges, have been suggested by pump-light ray tracing performed on the amplifier.

Extensive ray tracing was performed as part of the design of this amplifier. A fully three-dimensional, time-instantaneous, Monte-Carlo ray-trace code[15] was used to model the transport of energy from the flash lamps to the laser disks. Symmetry in the amplifier was used to reduce the ray-tracing problem to only one quadrant of the amplifier. Two million rays at 200 wavelengths were traced in a typical single-quadrant calculation. *S*- and *P*-averaged polarization properties were used. Flash lamps were accurately modeled as volume absorber-emitters using the Trenholme-Emmett-Jancaitis flash-lamp model.[16] Spatial resolution of the energy deposition in the glass was treated by dividing the disks into many volume segments, each of which is assigned the measured absorption spectrum of the Nd:glass. To obtain the actual stored energy at any segment within the model it was only necessary to normalize to the measured center-line stored

energy. Small-signal-gain results are obtained by tracing a fan of rays on either the horizontal or vertical diameters of the clear aperture through the disks using the predicted stored energies in the disk segments to calculate the gain.

The small-signal-gain results on the horizontal diameter are replotted in Fig. 49.31 along with the ray-tracing predictions. Since the ray-tracing results are inherently statistical, they are plotted as a band, which represents the $\pm 1\sigma$ ($\pm 3\%$) confidence limits associated with the results. The agreement is excellent over the majority of the clear aperture. The gain at the very edges of the aperture is sensitive to the details of the ends of the short-(end) pump modules and short-pump-module reflectors. In particular, modeling shows that changing the edges of the short-pump modules from wrapping around the last lamp to a simple 45° angle improves the horizontal gain profile near the edge. It is hypothesized that the edge gain is similarly sensitive to the treatment of the edges of the blast shields and their retainers, which have not been fully included in this model. Inclusion of this detail may result in closer agreement for the end points.

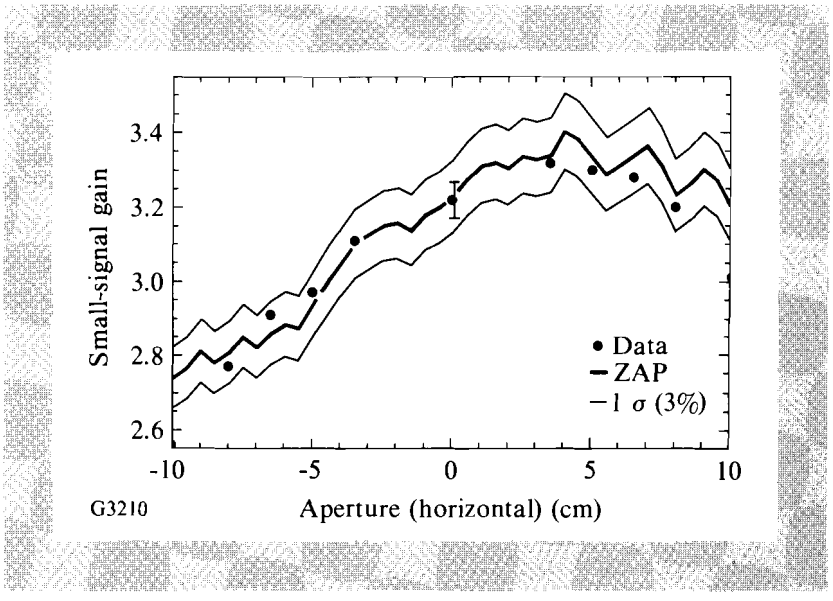

Fig. 49.31
The gain data on a horizontal diameter of Fig. 49.30 replotted along with the ray-tracing predictions. Note that the ray-tracing predictions are plotted as a band representing the $\pm 1\sigma$ confidence limits.

Further detailed examination of the model results for the horizontal diameter confirms that the variation is virtually entirely because of nonuniform pumping of the end disks. The interior disks are uniformly pumped on the horizontal diameter to $\pm 1\%$.

The gain in the vertical direction is very uniform until the edge of the aperture is approached. This is as expected since movement in the vertical direction accesses regions of the end disks at the same distance from the lamps. Variation can only occur close to the edge of the aperture where the glass is "shaded" by the disk holder.

Figure 49.32 replots the vertical-diameter gain data along with the ray-tracing predictions versus radial position. In this plot the upper and lower gain data sets have been averaged together. The ray tracing predicts a "horn" near the edge of

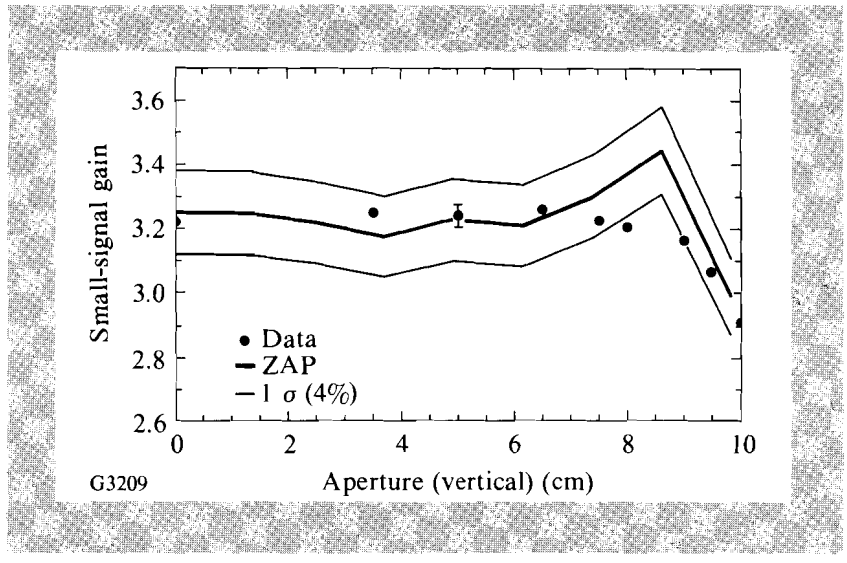

Fig. 49.32
The gain data on a vertical diameter of Fig. 49.30 replotted along with the ray-tracing predictions. Note that the ray-tracing predictions are plotted as a band representing the $\pm 1\sigma$ confidence limits.

the aperture. The data is much more uniform and does not display a similar increase. Further simulations are planned to investigate this.

Also shown on the plots in Fig. 49.30 are a polynomial fit $g_h(x)$ to the horizontal and a polynomial fit $g_v(y)$ to the vertical data. If the gain variation at the very edge of the aperture is assumed to be rotationally symmetric, and is assumed to be accurately represented by the measurements made along the vertical diameter, then an estimate of the gain in the entire aperture can be obtained. Let $g_v(y)$ be the gain measured on the vertical diameter and $g_h(x)$ be the gain measured on the horizontal diameter. Let $g(x,y)$ be the estimated gain at location (x, y) in the aperture. Then

$$g(x,y) = \frac{g_h(x)}{g_v(y)} g_v(r) ,$$

where $r = \sqrt{x^2 + y^2}$ is simply the radius. The function $g(x, y)$ is plotted in Fig. 49.33. If the log of this function is integrated over the total aperture area, the total stored energy in the amplifier may also be estimated. Using a stimulated-emission cross section of 3.5×10^{-20} cm^2, the total stored energy is 3.61 kJ. The storage efficiency η defined by

$$\eta = \frac{\text{total stored energy}}{\text{energy in bank}} = 1.7\% .$$

The small-signal performance of this amplifier meets or exceeds the requirements[17] for the OMEGA Upgrade. It achieved the required stored-energy density of 0.41 J/cm^3. The amplifier exceeded the required storage efficiency of 1.14% with adequate gain uniformity across the aperture.

Large-Signal Gain

To measure its large-signal gain, the amplifier was deployed as an additional final amplifier on one beamline of the OMEGA laser system. The original OMEGA beamline final amplifiers, 9.0-cm-diam rod amplifiers, routinely

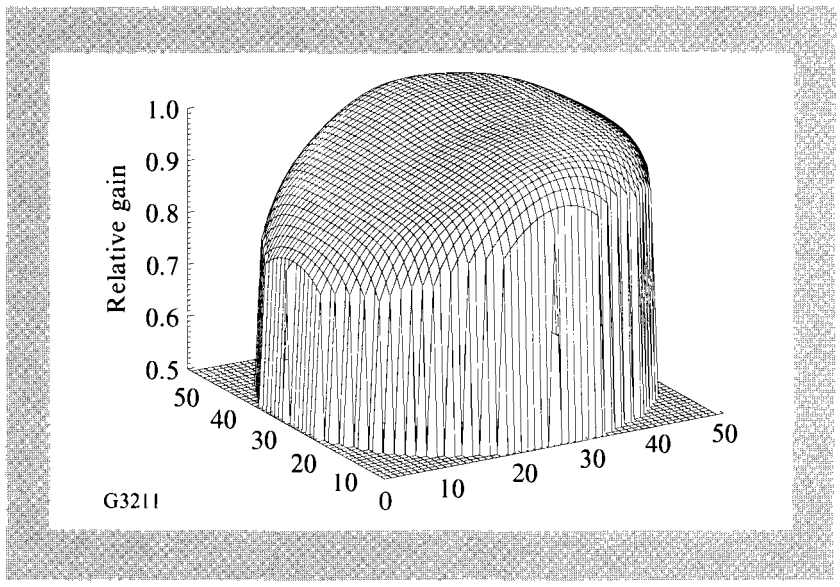

Fig. 49.33
Single-pass, small-signal-gain approximation function versus x-y location in the clear aperture. This gain was averaged over the area occupied by the in-coming and out-going beams in the center of the amplifier. The average gain thus calculated was used as an input for the RAINBOW code.

deliver over 120 J per beam in a 750-ps pulse. Since the disk amplifier is designed to operate with 300 to 350 J of input drive energy, it was necessary to angularly double pass with an input beam of significantly smaller diameter (~16 cm) than the clear aperture (20 cm). Although the beam size is reduced by this technique, the output fluences are comparable to those envisioned for actual use. A schematic of the experimental setup is shown in Fig. 49.34.

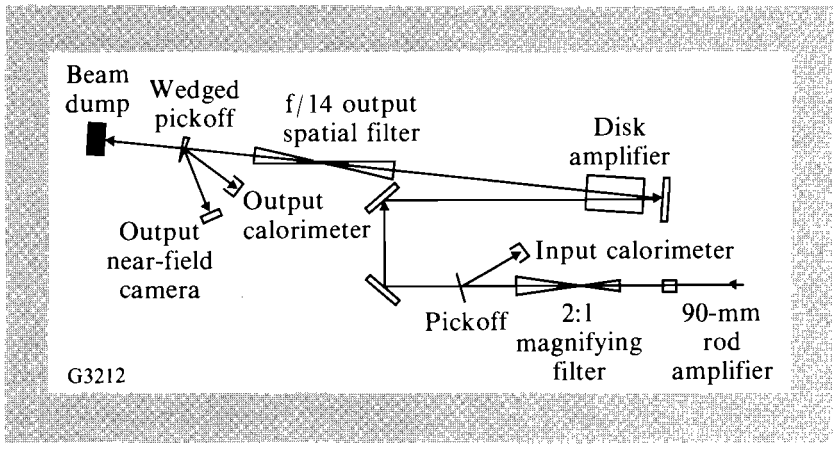

Fig. 49.34
Schematic of the large-signal-gain setup. The output of beamline 6-4 was turned and double passes the amplifier. All output diagnostics are located after the output spatial filter.

The output of beamline 6-4 was reflected to the amplifier by a mirror pair located just after the OMEGA output calorimeter pickoff. This allowed use of the existing OMEGA calorimetry system to measure input energy to the amplifier. This calorimeter was calibrated to read disk-amplifier input energy directly by comparison with a whole-beam calorimeter temporarily placed after the mirror pair. The beam propagates ~14 m from the mirror pair to the amplifier to permit the input and output beams to separate.

The beam was reflected for the second pass through the amplifier by a normal-incidence high reflector placed 73 cm from the corner of the nearest disk. This

resulted in the minimum delay between passes for any part of the amplifier of 4.8 ns. The maximum delay between passes for any part of the amplifier is 15.4 ns. Yarema and Milam[18] demonstrated only a small change in the saturation fluence with a pulse-width change of 1.4 to 20 ns. Since the delays between passes for any part of the amplifier fall within this range, lower lasing-level relaxation effects can be ignored in modeling this configuration.

The output beam propagated ~15 m to a 3-m focal length, 1:1 magnification spatial filter. For all of the tests performed, the cutoff half-angle in this filter was 400 μrad. All output diagnostics were located after the spatial filter (refer to Fig. 49.34). The second surface reflection from a wedge was used for the output calorimeter. The first surface reflection was used for output-beam, near-field photography.

All large-signal gains were measured with the amplifier at 80% of nominal capacitor-bank energy. The chosen bank energy corresponded to a center-line, small-signal gain of approximately 3.22. Three series of measurements were made, each with different beam spectral characteristics: transform-limited 740-ps pulses, 5-Å-bandwidth, FM-modulated 740-ps pulses, and angularly dispersed, frequency-modulated (SSD),[19] 740-ps pulses. Each "measurement" in one of the series actually consisted of three separate submeasurements. The first was an OMEGA shot to take a near-field photograph of the input beam at the requested drive energy. This measurement could not be made simultaneously with the gain measurement by use of a pickoff because of the resulting low-energy density on the film. The second submeasurement was of the actual input and output energies with the amplifier firing. The third submeasurement was of the input and output energies with the amplifier not fired in order to monitor the passive transmission of the entire stage including the mirrors and spatial filter. This yielded the transmission of the stage for use in modeling and served as a check for any possible misalignments.

The results of the first series with conventional transform-limited pulses is shown in Fig. 49.35. The actual data points are shown as crosses. The error bars in the vertical direction are the $\pm 3\sigma$ ($\pm 1.5\%$) confidence limits associated with the output calorimeter. The error bars in the horizontal direction are the $\pm 3\sigma$ confidence limits associated with the input calorimeter. Data extends up to an output energy of just over 700 J, corresponding to an output fluence (normal to the beam) of 3.5 J/cm^2. The maximum output fluence contemplated for this amplifier in the OMEGA Upgrade is 4.0 J/cm^2.

Also shown on this plot are the predictions of the laser energy-transport code RAINBOW.[20] This azimuthally-symmetric ray-tracing code features a modified Frantz-Nodvik[21] treatment of gain saturation that includes linear absorption in the laser glass and the saturation fluence model of Martin and Milam.[22] The required inputs to the model are the small-signal gain, the passive losses, the input beam fluence, and the saturation fluence.

The small-signal gain was measured during each gain shot by double passing a cw probe beam from the previously described small-signal-gain apparatus through the amplifier at a high angle so that the probe-beam collection optics did

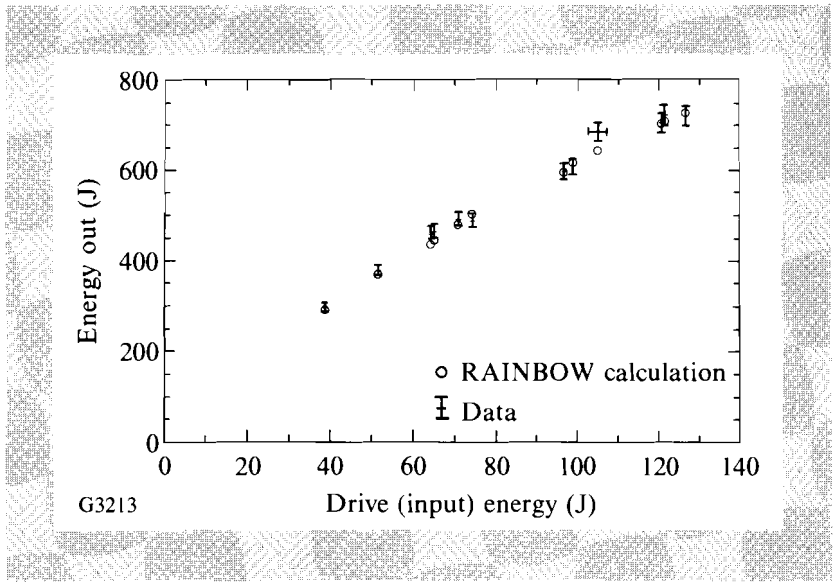

Fig. 49.35
Double-pass output energy in joules versus input drive energy in joules for transform-limited pulses. The open circles are the RAINBOW predictions.

not intercept the extracting beam. This not only allowed monitoring of the small-signal gain on each shot but also allowed verification of the timing of the extracting pulse relative to the temporal gain profile by observation of the gain saturation. The gain measured this way was corrected by a known ratio to yield the equivalent center-line-measured, small-signal gain. This center-line gain was used to normalize the spatial plot of gain shown in Fig. 49.33. A spatial average was then taken over an area equal to that of the overlapped beams in the center of the amplifier. This spatially averaged, small-signal gain was then used as input to the code for each simulation.

Since the passive losses were not expected to change over the course of the experiment (the alignment was left undisturbed), the average of all the transmission measurements was used to compute a single passive loss of the stage. The stage included the double-passed amplifier, three mirrors, and the output spatial filter. This loss was used for all simulations. The average passive loss for the stage was measured to be 0.937±0.023. In the simulations, this loss was distributed through the amplifier as a 0.00226 cm^{-1} loss. Approximately 1/3 of this loss may be attributed to the actual base-glass absorption, which is specified to be less than 0.0015 cm^{-1} at 1.05 μm per disk. The remainder is hypothesized to be caused by birefringence and scattering losses. The passive transmission in double pass for the entire stage is greater than the specified passive transmission for the amplifier alone (0.96) squared to account for double passing, 0.922.

The input beam fluences were deduced from the input calorimetry and the near-field photographs of the OMEGA output taken at the same energy. The film[23] data was digitized and density-to-intensity corrected by use of a separately generated D-log(I) curve for the same pulse width and wavelength. The average intensity $< I >$ on the film was calculated by

$$< I > = \int_0^\infty I \frac{dE}{dI}\, dI \Big/ \int_0^\infty \frac{dE}{dI}\, dI \ .$$

where dE/dI is the fraction of energy in the intensity range dI at the intensity I. The average beam-fluence (F_{avg}) input to the code was then calculated from

$$F_{avg} = \tau < I > ,$$

where τ is the temporal pulse width. Since dE/dI is not a delta function in the input near fields because of both beam modulation and the not-infinitely-steep beam edges, the simulations were all performed with an 18th-order superGaussian beam-edge profile to better approximate the actual beam shape. A perspective plot of a typical input near field that has been density-to-intensity converted is shown in Fig. 49.36.

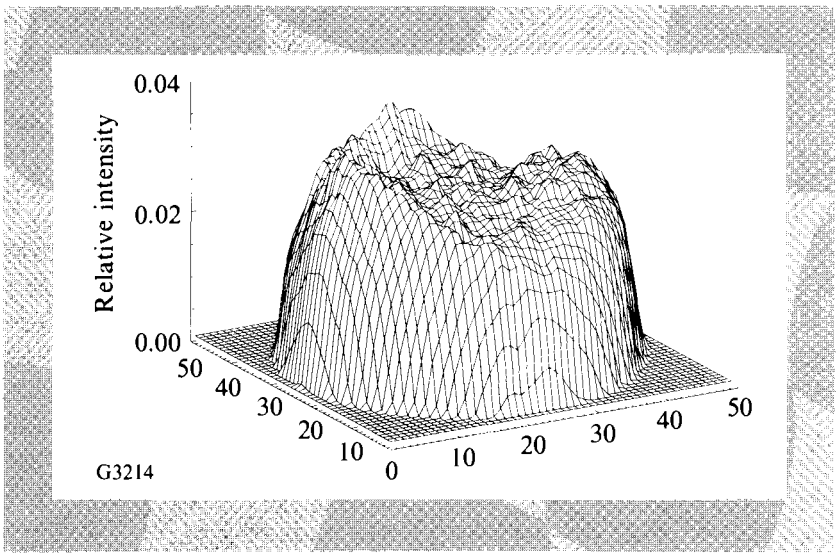

Fig. 49.36
Perspective plot of a density-to-intensity converted near field taken at the input to the amplifier. The z axis is relative intensity and the x and y axes are relative position. The input pulse is very nearly flat-topped. This is a transform-limited pulse with 51.2-J energy.

The saturation fluence F_{sat} is a function of both the glass type and the total fluence. All four disks were of phosphate glass; two were of Hoya[24] LHG-8 and two of Schott[25] LG-750. These two glass types have similar lasing properties. The saturation fluence for these glasses has been measured to be a function of the extracting fluence. This effect is caused by the inhomogeneous broadening of the ${}^4F_{3/2}$ to ${}^4I_{11/2}$ transition. A simplified explanation is as follows: The Nd^{+3} ions have some cross section and central wavelength distribution. The ions with a larger cross section and better wavelength match to the extracting beam are more readily depleted. The remaining ion population has a lower effective cross section and is a poorer spectral match resulting in a higher saturation fluence. The most recent saturation fluence data for these glass types is that of Yarema and Martin[18]

$$LHG-8\text{: } F_{sat} = 3.38 + 0.555 \ln(F_{out}) \text{ J/cm}^2$$
$$LG-750\text{: } F_{sat} = 3.88 + 0.313 \ln(F_{out}) \text{ J/cm}^2 ,$$

where F_{out} is the output fluence of their amplifiers that had small-signal gains of 4 to 5. For this work, a computationally simpler form based on fits to earlier 1-ns data[22] for LHG-8 was used for both glass types:

$$F_{\text{sat}}(t) = 3.75 + 0.032 \int_{-\infty}^{t} I(t')dt' \text{ J/cm}^2 ,$$

where t is the time of the current photon.

In Fig. 49.35, with the exception of three data points, all RAINBOW predictions fall within the error bars of the measurement. Considering the number of approximations inherent in the simulations this agreement is excellent. In the three exceptions, the code estimates are conservative, which is desirable in a design tool. RAINBOW also calculates the maximum ΔB through the stage. The maximum calculated ΔB for all three series occurred on the 720-J output shot and was 0.89 rad. This is the same value that is anticipated for actual use on the OMEGA Upgrade.

In the second series of measurements, an FM modulation was applied to the 740-ps pulse using an electro-optic modulator.[26] The resulting bandwidth consisted of a 5 Å "comb" of sidebands each separated by 9.65 GHz. The 5-Å bandwidth is of the same order as the 7.5-Å bandwidth planned for the OMEGA Upgrade.[27] Reduction in the large-signal gain because of a decrease in the small-signal gain experienced by the wings of the spectrum is not expected since the 5-Å bandwidth is small compared to both the fluorescence linewidth of these glasses (~230 Å) and the 3-db-gain bandwidth of the amplifier in double pass (~100 Å). No increase in extraction is expected because of the increased bandwidth of the extracting beam accessing more of the inhomogeneously broadened line since the 5-Å bandwidth is small compared to the homogeneous linewidth[28] (~24 Å for LG-750, LHG-8 expected to be similar).

The results of the second series of measurements are shown in Fig. 49.37. Again, output energy is plotted versus drive energy in joules. Also shown again are the RAINBOW simulations. All of the predictions fall within the error bars

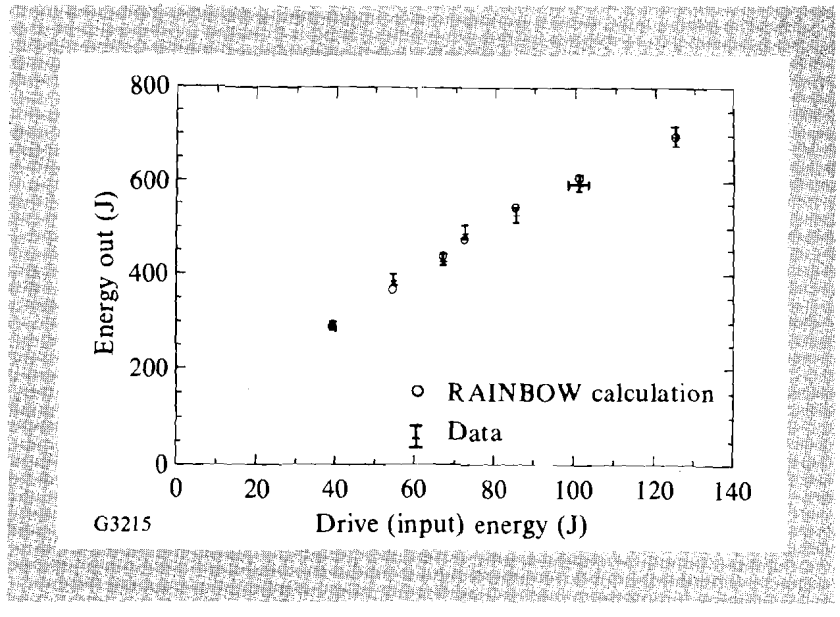

Fig. 49.37
Double-pass output energy in joules versus input drive energy in joules for FM-modulated pulses. The open circles are RAINBOW predictions for transform-limited pulses of the same energy. The differences between predictions that do not take into account bandwidth and the data are within the error bars of the measurement. This is as expected because the FM bandwidth is still small relative to the published homogeneous linewidth of LG-750. LHG-8's homogeneous linewidth is expected to be similar, because of the similarity in glass composition.

of the measurement. Since bandwidth has been ignored in these simulations it may be concluded that within the error bars of these measurements, 5-Å-FM bandwidth has no effect on the large-signal gain of this amplifier.

The third and final series of measurements were made with spatially-dispersed, FM-modulated (SSD), 740-ps pulses. The same FM modulator was used as in the previous series. A grating after the modulator angularly disperses the FM-modulated light by 67 μrad/Å in the vertical direction at the amplifier stage. Data in this series were limited to drive energies <75 J because of the low diffraction efficiency of the prototype grating used as the dispersing element. In addition, the near-field beam quality was degraded because of grating imperfections. The results are shown in Fig. 49.38 along with the RAINBOW simulations. The three predictions underestimate the output energy, one significantly. This is attributed to a low, small-signal-gain measurement caused by poor utilization of the range of the *A*-to-*D* converters in the digitizing oscilloscopes. No effect on energy transport can be attributed to the spatial dispersion.

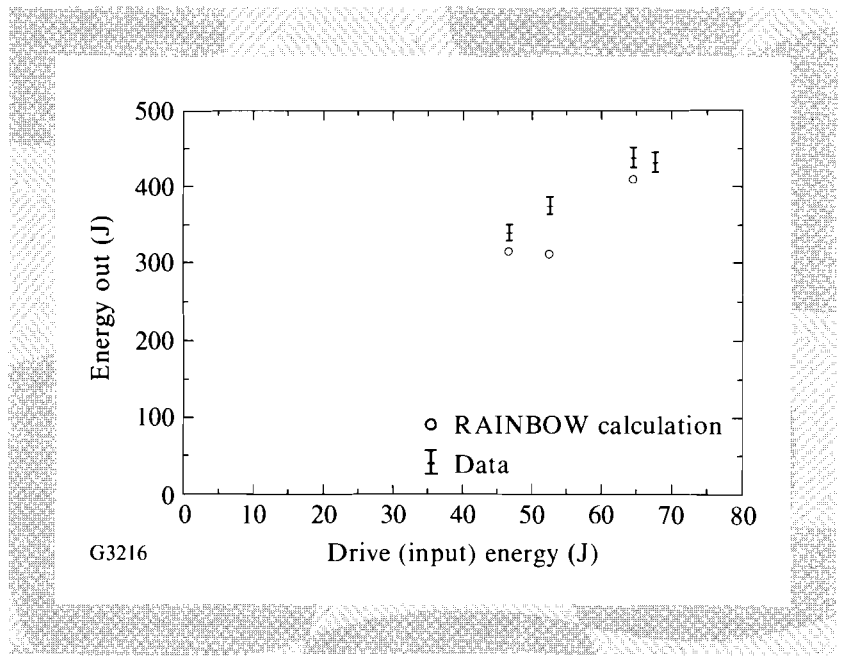

Fig. 49.38
Double-pass output energy in joules versus input drive energy in joules for spatially dispersed FM-modulated pulses. The open circles are RAINBOW predictions for transform-limited pulses of the same energy.

Conclusion

The OMEGA Upgrade will use a modern, 20-cm clear aperture, Nd:glass Brewster-disk amplifier as the final amplifier. This device has been designed, constructed, characterized, and it has met or exceeded its design goals in all aspects of energy transport. These goals are summarized in Table 49.V. Specifically, it achieved a small-signal gain of 3.22 at only 80% of design bank energy with a storage efficiency of 1.7%. Passive losses are consistent with the values assumed for the OMEGA Upgrade. The amplifier has been tested in the large-signal regime by double passing at a pulse width of 740 ps. It produced over 720 J of energy with 126-J drive at an output fluence of 3.5 J/cm^2. Wavefront characterization results will be presented in a future article.

Table 49.V: 20-cm-disk amplifier performance.

	Goal	Achieved
Center-line small-signal gain	3.0	3.22
(at) bank energy	300 kJ	240 kJ
Gain G uniformity at center-line gain G_{CL}	$2.7 < G < 3.3$ $G_{CL} = 3.00$	$2.57 < G < 3.32$ $G_{CL} = 3.22$
Storage efficiency	1.14%	1.7%
Passive transmission	0.922 double pass amplifier only	0.937 double pass entire stage
Output energy	1050 J	730 J drive limited
(at) max output fluence	4.0 J/cm^2	3.5 J/cm^2 drive limited

G3230

ACKNOWLEDGMENT

This work was supported by the U.S. Department of Energy Office of Inertial Confinement Fusion under agreement No. DE-FC03-85DP40200 and by the Laser Fusion Feasibility Project at the Laboratory for Laser Energetics, which is sponsored by the New York State Energy Research and Development Authority and the University of Rochester.

REFERENCES

1. We are grateful for the cooperation of our colleagues at Lawrence Livermore National Laboratory; especially Dr. H. T. Powell, Dr. J. E. Murray, and Dr. A. T. Erlandson.
2. Rutherford Appleton Laboratory Annual Report to the Laser Facility Committee, pp. A6.6–A6.12, (1985).
3. S. M. Yarema and J. E. Murray, Lawrence Livermore National Laboratory Laser Program Annual Report 1980, UCRL 50021-80 (1981), pp. 2-234–2-244.
4. Private communication from K. Moncur, KMS Fusion, Inc., 1989.
5. Lawrence Livermore National Laboratory Laser Program Annual Report 1986, UCRL 50021-86 (1987), pp. 4-14–4-59.
6. LLE Review **44**, 205 (1990).
7. M. J. Shoup III, J. H. Kelly, M. M. Tedrow, F. A. Rister, and K. Thorp, "Mechanical Design of 15- and 20-cm Clear Aperture Disk Amplifiers for the OMEGA Upgrade," presented at the *SPIE's OE-LASE '92 Technical Conference on High-Power Lasers*, Los Angeles, CA, 20–25 January 1992.

8. M. Andre *et al.*, "High Energy Laser System Development at 'Centre D'Etudes de Limeil' in France," presented at the *IAEA Technical Committee Meeting on Drivers for Inertial Confinement Fusion*, Osaka, Japan, 15–19 April 1991.

9. Dr. J. E. Murray of Lawrence Livermore National Laboratory developed this technique.

10. Tektronix Inc., Beaverton, Oregon, USA. Reference to a company or a product name does not imply approval or recommendation of the product by the University of Rochester or the U.S. Department of Energy.

11. R. B. Blackman and J. W. Tukey, *The Measurement of Power Spectra,* in *The Point of View of Communications Engineering* (Dover Publications, New York, 1958).

12. Dr. K. Jancaitis of Lawrence Livermore National Laboratory modeled the parasitic characteristics of these disks prior to their fabrication and predicted that there would be no self-oscillation.

13. LLE Review **37**, 16 (1988).

14. J. E. Murray, H. T. Powell, and B. W. Woods, "Optimized Flash-lamp Pumping of Disc Amplifiers," presented at *SPIE's OE/LASE '86 Conference*, Los Angeles, CA, 19–24 January 1986. Available as preprint UCRL-93321 from Technical Information Department, Lawrence Livermore National Laboratory, P.O. Box 808, Livermore, CA 94550.

15. The code used is a greatly updated and enhanced version of the code ZAP originally written by Systems, Science and Software for the Naval Research Lab by J. H. Alexander, M. Troost, and J. E. Welch, ARPA order number 660, Contract number N00014-70-C-0341, 1971.

16. K. S. Jancaitis and H. T. Powell, "An Empirical Model for Predicting the Absolute Radiative Emission and Absorption Spectra of Xenon Flash Lamps." Available as preprint UCID-21226 from Technical Information Department, Lawrence Livermore National Laboratory, P.O. Box 808, Livermore, CA 94550.

17. R. S. Craxton, Ed., *OMEGA Upgrade Preliminary Design*, Laboratory for Laser Energetics Report DOE/DP 40200-101, University of Rochester, pp. 6.28–6.30, 1989. Note that the performance numbers in this document are based on the earlier value for the stimulated-emission cross section of 4.0×10^{-20} cm^2.

18. S. M. Yarema and D. Milam, IEEE J. Quantum Electron. **18**, 1941 (1982).

19. S. Skupsky, R. W. Short, T. Kessler, R. S. Craxton, S. Letzring, and J. M. Soures, J. Appl. Phys. **66**, 3456 (1989).

20. D. C. Brown, "Simulation and Modeling of Small-Scale Self-Focusing Effects," in *High-Peak-Power Nd:Glass Laser Systems* (Springer-Verlag, New York, 1981), Sec. 7.7, p. 229.

21. L. M. Frantz and J. S. Nodvik, J. Appl. Phys. **34**, 2346 (1963).

22. W. E. Martin and D. Milam, IEEE J. Quantum Electron. **18**, 1155 (1982).

23. The film used was Kodak type 4143 IR film. Reference to a company or a product name does not imply approval or recommendation of the product by the University of Rochester or the U.S. Department of Energy.

24. Hoya Optics, Inc., 3400 Edison Way, Fremont, CA 94538-6190. Reference to a company or a product name does not imply approval or recommendation of the product by the University of Rochester or the U.S. Department of Energy.

25. Schott Glass Technologies, Inc., 400 York Avenue, Duryea, PA 18642. Reference to a company or a product name does not imply approval or recommendation of the product by the University of Rochester or the U.S. Department of Energy.

26. LLE Review **37**, 29 (1988).

27. R. S. Craxton, Ed., *OMEGA Upgrade Preliminary Design*, Laboratory for Laser Energetics Report DOE/DP 40200-101, University of Rochester, pp. 3.21–3.24, 1989.

28. D. W. Hall, M. J. Weber, and R. T. Brundage, J. Appl. Phys. **55**, 2642 (1984).

Section 3
NATIONAL LASER USERS FACILITY NEWS

NLUF activity for the first quarter of FY92 was centered around experiments conducted on GDL. These were done by groups from the National Institute of Standards and Technology (NIST), the Naval Research Laboratory (NRL), and the University of Maryland.

J. Reader from NIST has set up a high-resolution XUV spectrograph to measure the line radiation from laser-produced plasmas. These spectral measurements are a continuation of measurements made during the last quarter. This instrument continues to provide some of the highest resolution measurements of line radiation from laser-produced plasmas to date. It is expected that there will be at least one more set of exposures taken before the instrument is returned to NIST.

R. Whitlock from NRL conducted a series of experiments with the GDL laser to study the effect of thermal shock waves on the lattice spacing of crystalline materials. X rays from a laser-plasma source were used to probe the lattice-spacing change of the crystal as the shock wave propagated from the front surface to the rear surface. These experiments were done in collaboration with **J. Wark** from the University of Oxford. These shots were sufficient to complete the data-acquisition phase of this NLUF experiment.

J. Moreno from the University of Maryland made use of the McPhearson grazing-incidence spectrograph to measure several high-resolution spectra from

carbon targets. **H. Griem's** group at the University of Maryland is studying line shapes of hot dense plasmas. These shots on GDL complement the data that has been collected off OMEGA with both imploding and non-imploding targets.

The American Physical Society's Division of Plasma Physics meeting was held in Tampa, Florida from 4 November through 8 November. Papers on work done as part of the NLUF program were presented by groups from the University of Maryland, the University of Florida, and the University of California at Davis. We would like to congratulate H. Griem from the University of Maryland for receiving the James Clark Maxwell Prize for Plasma Physics at this year's meeting. Prof. Griem was honored for his outstanding contributions to the measurement of x-ray spectra from plasmas.

ACKNOWLEDGMENT

This work was supported by the U.S. Department of Energy Office of Inertial Confinement Fusion under agreement No. DE-FC03-85DP40200.

Section 4
LASER SYSTEM REPORT

4.A GDL Facility Report

There was a total of 320 GDL laser shots during the first quarter of FY92. The 142 target shots were used by one LLE experiment and three NLUF user experiments. The NLUF user experiments were done by groups from the National Institute of Standards and Technology, the Naval Research Laboratory, and the University of Maryland. In addition, construction was started on a spatial filter that will be used to transport the GDL laser beam into the LLE Damage Testing Laboratory. This is a UV spatial filter that will allow the testing of large-scale UV optics.

The decision was made this quarter to do a major refurbishment of the GDL facility. The work will start in June of 1992 and continue for approximately nine months. Both the laser and the experimental target bay are to be improved and will provide users with a better experimental facility.

The shot summary for the GDL laser this quarter is as follows:

Laser system		148
Laser calibration		30
Target		142
	TOTAL	320

4.B OMEGA Facility Report

There was a total of 265 OMEGA laser shots during the first quarter of FY92. The 65 target shots were delivered to three experiments in preparation for the American Physical Society's Division of Plasma Physics meeting. These experiments were done to study the effect of low-order, ℓ-mode illumination nonuniformity, the implosion of surrogate cryogenic targets (CD shells), and laser-system performance characterization. The smoothing by spectral dispersion apparatus was removed for these shots while a new set of gratings is being manufactured. The temporal shape of the laser beams was Gaussian for the target shots.

The OMEGA driver line continued its progress toward the ability to deliver shaped pulses to the input of OMEGA. A beam from the pulse-shaping equipment was injected into the OMEGA driver line and the optical-component alignment was started. Diagnostics to sample the spatial beam profile at various image planes in the driver line were added and a streak camera was set up to measure the temporal profile of the laser beam at the output of the driver line. This will be finished during the next quarter when the new gratings are to be mounted and a modulator with a new crystal installed.

The shot summary for the OMEGA laser this quarter is as follows:

Software test		20
Driver		141
Laser		39
Target		65
	TOTAL	265

ACKNOWLEDGMENT

This work was supported by the U.S. Department of Energy Office of Inertial Confinement Fusion under agreement No. DE-FC03-85DP40200 and by the Laser Fusion Feasibility Project at the Laboratory for Laser Energetics, which is sponsored by the New York State Energy Research and Development Authority and the University of Rochester.

PUBLICATIONS AND CONFERENCE PRESENTATIONS

Publications

S. Augst, D. D. Meyerhofer, J. Peatross, and C. I. Moore, "Spatial Distribution of High-Order Harmonics Generated in the Tunneling Regime," in the *Proceedings of the Topical Meeting on Short-Wavelength Coherent Radiation: Generation and Application*, edited by P. H. Bucksbaum and N. M. Ceglio (Optical Society of America, Monterey, CA, 1991), Vol. II, pp. 23–27.

H. Chen, Y.-H. Chuang, J. A. Delettrez, S. Uchida, and D. D. Meyerhofer, "Study of X-Ray Emission from Picosecond Laser-Plasma Interaction," in *Short-Pulse High-Intensity Lasers and Applications*, edited by H. A. Baldis (SPIE, Bellingham, WA, 1991), Vol. 1413, pp. 112–119.

Y.-H. Chuang, J. Peatross, and D. D. Meyerhofer, "Modeling the Pedestal in a Chirped-Pulse-Amplification Laser," in *Short-Pulse High-Intensity Lasers and Applications*, edited by H. A. Baldis (SPIE, Bellingham, WA, 1991), Vol. 1413, pp. 32–40.

J. Delettrez, R. Epstein, D. K. Bradley, P. A. Jaanimagi, R. C. Mancini, and C. F. Hooper, "Hydrodynamic Simulations with Non-LTE Atomic Physics of High-Density Implosions of Argon-Filled Polymer Shell Targets," in *Radiative Properties of Hot Dense Matter, Proceedings of the 4th International Workshop*, edited by W. Goldstein, C. Hooper, J. Gauthier, J. Seely, and R. Lee (World Scientific, NJ, 1991), pp. 309–320.

W. R. Donaldson, "Optical Probing of Field Dependent Effects in GaAs Photoconductive Switches," in the *Proceedings of the 8th IEEE International*

Pulsed Power Conference, edited by R. White and K. Prestwich (IEEE, NY, 1991), pp. 45–49.

E. M. Epperlein, "Kinetic Simulations of Laser Filamentation in Plasmas," Phys. Fluids B **3**, 3082 (1991).

E. M. Epperlein and R. W. Short, "A Practical Nonlocal Model for Electron Heat Transport in Laser Plasmas," Phys. Fluids B **3**, 3092 (1991).

E. M. Epperlein, "Electron Kinetics in Laser-Driven Inertial Confinement Fusion," in *Research Trends in Physics: Nonlinear and Relativistic Effects in Plasmas*, edited by V. Stefan (American Institute of Physics, New York, 1991), p. 43.

R. Epstein and B. Yaakobi, "Effect of Photoelectric Fluorescence on the Formation of X-Ray Absorption Lines in Laser Plasma Experiments," Phys. Rev. A **44**, 5111 (1991).

P. M. Fauchet, D. A. Young, W. L. Nighan, Jr., and C. M. Fortmann, "Picosecond Carrier Dynamics in a $Si_{0.5}Ge_{0.5}$:H Measured With a Free Electron Laser," IEEE J. Quantum Electron. **27**, 2714 (1991).

T. Gong and P. M. Fauchet, "Femtosecond Refractive and Absorptive Nonlinearities Due to Real Carriers in GaAs," in the *OSA Proceedings on Picosecond Electronics and Optoelectronics*, edited by T. C. L. G. Sollner and J. Shah (Optical Society of America, Washington, DC, 1991), Vol. 9, pp. 253–259.

A. Honig, N. Alexander, Q. Fan, R. Q. Gram, and H. Kim, "Absence of Molecular Deuterium Dissociation During Room-Temperature Permeation into Polystyrene Inertially Confined Fusion Target Shells," J. Vac. Sci. Technol. A **9**, 3149 (1991).

C. J. McKinstrie and M. Yu, "The Role of Ion Momentum in Stimulated Raman Scattering," Phys. Fluids B **3**, 3041 (1991).

S. Nakai, J. M. Soures, K. Ueda, R. N. Sudan, and G. Velarde, "Drivers for Inertial Confinement Fusion," *Report on the IAEA Technical Committee Meeting*, Osaka, Japan, 15–19 April 1991, Nucl. Fusion **31**, 2005 (1991).

D. Y. Park, W. D. Seka, Y. Lin, and D. L. Brown, "Operational Characteristics of an Imaging, Unstable Ring Resonator Using Nd:YLF as Active Medium," in the *Proceedings of the International Conference on Lasers '89*, New Orleans, LA, 3–8 December 1989 (STS Press, McLean, VA, 1990), pp. 450–456.

R. Sobolewski, "Ultrafast Superconducting Electronics," in *Semiconductor Equipment and Technology (Invited Papers)*, edited by A. Bakowski (Hi-Tech Co., Ltd., Warsaw, Poland, 1991), pp. 130–140.

Y. Wang, B. Luther-Davies, Y.-H. Chuang, R. S. Craxton, and D. D. Meyerhofer, "Highly Efficient Conversion of Picosecond Nd Laser Pulses With the Use of Group-Velocity-Mismatched Frequency Doubling in KDP," Opt. Lett. **16**, 1862 (1991).

M. D. Wittman, D. Malacara, and H.-J. Kong, "High Precision Characterization of Gas-Filled Shells Using Scanning Fabry-Perot Interferometry," in *Laser*

Interferometry IV: Computer-Aided Interferometry (SPIE, Bellingham, WA, 1991), Vol. 1553, pp. 456–469.

B. Yaakobi, R. Epstein, and F. J. Marshall, "Diagnosis of Laser-Compressed Shells Based on Absorption of Core Radiation," Phys. Rev. A **44**, 8429 (1991).

Forthcoming Publications

S. Alexandrou, R. Sobolewski, and T. Y. Hsiang, "Bend-Induced Even and Odd Modes in Picosecond Electrical Transients Propagated on a Coplanar Waveguide," to be published in Applied Physics Letters.

T. R. Boehly, R. S. Craxton, R. J. Hutchison, J. H. Kelly, T. J. Kessler, S. A. Kumpan, S. A. Letzring, R. L. McCrory, S. F. B. Morse, W. Seka, S. Skupsky, J. M Soures, and C. P. Verdon, "The Upgrade to the OMEGA Laser System," to be published in the *Proceedings of SPIE's OE/LASE*, Los Angeles, CA, 20–25 January 1992.

P. C. Cheng, H. Kim, and T. H. Lin, "The Study of Silica Deposition in the Leaf Blade of Zea mays L. by X-Ray Contact Microradiography and Confocal Microscopy," to be published in *X-Ray Microscopy III*.

W. R. Donaldson and L. Mu, "The Effects of Doping on Photoconductive Switches as Determined by Electro-Optic Imaging," to be published in the *Proceedings of SPIE's OE/LASE*, Los Angeles, CA, 20–25 January 1992.

Conference Presentations

R. L. McCrory, "A Problem of Target Illumination Homogeneity in Laser Fusion," presented at the XIV International Conference on Coherent and Nonlinear Optics, Leningrad, USSR, 24–27 September 1991.

J. P. Chu, G. G. Banas, H. E. Elsayed-Ali, J. M. Rigsbee, and F. V. Lawrence, Jr., "Laser-Shock Hardening of Hadfield Steel," presented at the TMS Fall Meeting, The American Institute of Mining, Metallurgical, and Petroleum Engineering, Cincinnati, OH, October 1991.

T. Gong and P. M. Fauchet, "Femtosecond Nonlinearities and Hot-Carrier Dynamics in GaAs," presented at the VIIth International Symposium on Ultrafast Processes in Spectroscopy, Bayreuth, Germany, 7–11 October 1991 (invited paper).

M. J. Cumbo, A. Lindquist, S. B. Ng, T. Rich, Y. Sabharwal, and S. D. Jacobs, "Grinding of Optical Glass with Loose Polycrystalline Synthetic Diamond Abrasives," presented at the American Society for Precision Engineering Annual Meeting, Santa Fe, NM, 13–18 October 1991.

The following presentations were made at the 21st ECLIM, Warsaw, Poland, 21–25 October 1991:

R. L. McCrory, "Direct-Drive Implosion Experiments for Laser Fusion on OMEGA and the OMEGA Upgrade."

W. Seka, R. S. Craxton, R. Bahr, D. L. Brown, A. Simon, R. L. Short, and L. Zheng, "Nonlinear Interaction Processes in Long-Scale-Length Plasma Experiments on OMEGA."

J. M. Soures, R. L. McCrory, C. P. Verdon, T. R. Boehly, R. S. Craxton, S. D. Jacobs, J. H. Kelly, T. J. Kessler, J. P. Knauer, R. L. Kremens, S. A. Kumpan, S. A. Letzring, W. Seka, R. W. Short, M. D. Skeldon, and S. Skupsky, "Uniform Irradiation Laser Facility for Short-Wavelength Direct-Drive Target Experiments."

R. Sobolewski, "Ultrafast Superconducting Electronics," presented at the Second Mideuropean Symposium and Exhibition on Semiconductor Equipment and Technology, Warsaw, Poland, 22–24 October 1991 (invited lecture).

The following presentations were made at the 23rd Boulder Damage Symposium on Optical Materials for High Power Lasers, Boulder, CO, 23–25 October 1991:

S. Papernov, L. Pedulla, V. Zandy, A. W. Schmid, and P. Resnick, "Perfluorinated Copolymer Coatings for High-Power Laser Applications."

L. J. Shaw-Klein, S. D. Jacobs, S. J. Burns, and J. C. Lambropoulos, "Microstructural Control of Thin-Film Thermal Conductivity."

D. J. Smith, A. W. Schmid, M. S. Jin, S. Papernov, and Z. R. Chrzan, "Development of High Reflector Coatings at 351 nm for the OMEGA Upgrade Laser."

The following presentations were made at the Optical Society of America 1991 Annual Meeting, San Jose, CA, 3–8 November 1991:

J. H. Kelly, "Instrumentation Integration in Large Systems: the OMEGA Laser Upgrade at the University of Rochester as an Example," (invited talk).

A. W. Schmid, M. S. Kim, K. Cerqua, and W. C. LaCourse, "Self-Trapped Exciton Enhanced Photostructural Transformation in AsSe Fiber Glass."

D. J. Smith, M. S. Jin, Z. R. Chrzan, A. W. Schmid, and S. Papernov, "Improved Laser-Damage Thresholds Using Ion-Assisted Deposition."

The following presentations were made at the Thirty-Third Annual Meeting of the American Physical Society, Division of Plasma Physics, Tampa, FL, 4–8 November 1991:

R. E. Bahr, W. Seka, R. S. Craxton, and A. Simon, "Stimulated Raman Scattering in Long-Scale Length Plasma Experiments on OMEGA."

T. R. Boehly, R. S. Craxton, R. J. Hutchison, J. H. Kelly, T. J. Kessler, S. A. Kumpan, S. A. Letzring, R. L. McCrory, S. F. B. Morse, W. Seka, S. Skupsky, J. M. Soures, and C. P. Verdon, "The Upgrade to the OMEGA Laser System."

D. K. Bradley, P. W. McKenty, and C. P. Verdon, "Experimental Determination of Low Order Legendre Mode Growth Rates in Imploding ICF Targets."

D. L. Brown, R. E. Bahr, and W. Seka, "Interpretation of Features in Short-Pulse Probe Images of Long-Scale-Length Plasmas on OMEGA."

X. D. Cao, C. J. McKinstrie, and D. A. Russell, "Novel Aspects of the Nonlinear Focusing of Light Waves."

R. S. Craxton, W. Seka, and D. L. Brown, "Optical Diagnosis of Long-Scale-Length Plasmas on the OMEGA Upgrade."

J. A. Delettrez, D. K. Bradley, and C. P. Verdon, "Modeling Burnthrough Experiments with an Interactive Mix Model in *LILAC*."

E. M. Epperlein, "Fokker-Planck Simulations of Laser Filamentation in Plasmas."

E. M. Epperlein and R. W. Short, "A Practical Nonlocal Model for Electron Heat Transport in Laser Plasmas."

R. Epstein, C. T. Cotton, T. J. Kessler, and S. Skupsky, "The Effects of Phase Aberration on the Irradiation Uniformity and Focusability of Phase-Covered Laser Beams."

P. A. Jaanimagi, D. K. Bradley, and J. A. Delettrez, "X-Ray Emission in the Post-Stagnation Phase."

J. H. Kelly, P. W. McKenty, R. W. Short, and S. Skupsky, "Numerical Investigation of Self-Focusing of Broad Bandwidth Laser Light."

T. J. Kessler, T. R. Boehly, J. H. Kelly, S. A. Kumpan, S. A. Letzring, W. Seka, S. Skupsky, J. M. Soures, and C. P. Verdon, "Design Improvements for the OMEGA Upgrade Laser System."

R. L. Kremens and M. A. Russotto, "Wide Dynamic Range Measurement of Low Neutron Yields from Inertial Confinement Fusion Experiments Using Scintillator-Photomultiplier Detectors."

F. J. Marshall, J. A. Delettrez, C. P. Verdon, R. Epstein, and B. Yaakobi, "Absorption Spectroscopy of Imploding Hollow Shell Targets on OMEGA."

P. W. McKenty, C. P. Verdon, S. Skupsky, D. K. Bradley, P. A. Jaanimagi, and J. P. Knauer, "ICF-Target Performance Under the Influence of Low-Order Deliberately Applied Illumination Nonuniformities."

C. J. McKinstrie and M. Yu, "Momentum Conservation in Stimulated Raman Scattering."

M. A. Russotto and R. L. Kremens, "Fuel Ion Temperature and Neutron Yield Measurements Using the MEDUSA Neutron Detector Array."

W. Seka, "Long-Scale-Length Laser-Plasma Experiments Using the OMEGA Laser Facility."

W. Seka, D. L. Brown, R. E. Bahr, A. Simon, R. L. Short, E. M. Epperlein, and R. S. Craxton, "Evidence of Filamentation in Long-Scale-Length Plasma Experiments on OMEGA."

R. W. Short, "The Filamentation Instability in the Presence of Multiple Pump Waves."

A. Simon, "Brillouin Scattering in the Presence of Strong Ion Collisionality."

S. Skupsky, "Beam Smoothing and Pulse Shaping for Solid-State Lasers."

S. Skupsky, T. J. Kessler, and S. A. Letzring, "Laser-Beam Pulse Shaping by Spectral Deflection Techniques."

S. Uchida, H. Chen, Y.-H. Chuang, J. A. Delettrez, and D. D. Meyerhofer, "Superthermal Electrons and Ion Production in Picosecond Laser-Plasma Interactions."

B. Yaakobi, R. Epstein, and F. J. Marshall, "Diagnosis of Laser Compressed Shells Based on Absorption of Core Radiation."

H. Kim, J. M. Soures, P. C. Cheng, T. H. Lin, R. Acharya, G. Wang, W. S. Liou, W. S. Tarng, and J. K. Samarabandu, "Investigation of Inertial Fusion Target by Confocal Microscopy and X-Ray Microtomography," presented at the 38th Annual AVS Symposium & Topical Conference, Seattle, WA, 11–15 November 1991.

S. H. Chen, S. Krishnamurthy, and S. D. Jacobs, "Chemical Structure-Optical Property Relationships Involving Thermotropic Liquid Crystal Polymers Exhibiting Cholesteric Mesophase," presented at the American Institute of Chemical Engineers Meeting "Structured Polymer Liquids: Liquid Crystals, Micelles and Gels I, II, and III," Los Angeles, CA, 17–22 November 1991.

C. Twomey, S. H. Chen, and A. W. Schmid, "Complexation, Morphology, and Fluorescence Life Time Measurement of the Neodymium Doped Poly(ethylene oxide)," presented at the American Institute of Chemical Engineers Meeting, "Active, Smart, and Responsive Polymeric Materials," Los Angeles, CA, 17–22 November 1991.

J. C. Lambropoulos, S. D. Jacobs, S. J. Burns, L. Shaw-Klein, and S.-S. Hwang, "Thermal Conductivity of Thin Films: Measurement and Microstructural Effects," presented at the Heat Transfer in Solid Thin Films, 1991 ASME Winter Annual Meeting, Atlanta, GA, 1–6 December 1991.

ACKNOWLEDGMENT

The work described in this volume includes current research at the Laboratory for Laser Energetics, which is supported by New York State Energy Research and Development Authority, the University of Rochester, the U.S. Department of Energy Office of Inertial Confinement Fusion under agreement No. DE-FC03-85DP40200, and other agencies.

UNIVERSITY OF
ROCHESTER